Numer. Math. Theor. Meth. Appl. doi: 10.4208/nmtma.OA-2023-0007

A Physics-Informed Structure-Preserving Numerical Scheme for the Phase-Field Hydrodynamic Model of Ternary Fluid Flows

Qi Hong¹, Yuezheng Gong¹ and Jia Zhao^{2,*}

Received 12 January 2023; Accepted (in revised version) 20 April 2023

Abstract. Phase-field models are widely used in studying multiphase flow dynamics. Given the complexity and strong nonlinearity, designing accurate, efficient, and stable numerical algorithms to solve these models has been an active research field for decades. This paper proposes a novel numerical scheme to solve a highly cited and used phase field hydrodynamic model for simulating ternary phase fluid flows. The main novelty is the introduction of a supplementary variable to reformulate the original problem into a constrained optimization problem. This reformulation leads to several advantages for our proposed numerical algorithms compared with many existing numerical techniques for solving this model. First, the developed schemes allow more straightforward calculations for the hydrodynamic phase-field models by solving a few decoupled Helmholtz or Poisson-type systems with a constant precomputable coefficient matrix, remarkably reducing the computational cost. Secondly, the numerical schemes can maintain mass conservation and energy dissipation at the discrete level. Additionally, the developed scheme based on the secondorder backward difference formula respects the original energy dissipation law that differs from many existing schemes, such as the IEQ, SAV, and Lagrange multiplier approaches for which a modified energy dissipation law is respected. Furthermore, rigorous proof of energy stability and practical implementation strategies are provided. We conduct adequate 2D and 3D numerical tests to demonstrate the proposed schemes' accuracy and effectiveness.

AMS subject classifications: 52B10, 65D18, 68U05, 68U07

Key words: Energy stable, phase field, Cahn-Hilliard-Navier-Stokes, supplementary variable method.

School of Mathematics, Nanjing University of Aeronautics and Astronautics; Key Laboratory of Mathematical Modelling and High Performance Computing of Air Vehicles (NUAA), MIIT, Nanjing 211106, China
 Department of Mathematics and Statistics, Utah State University, Logan, UT, 84322, USA

^{*}Corresponding author. Email address: jia.zhao@usu.edu (J. Zhao)

1. Introduction

Multiphase flows exist ubiquitously in nature and arise in many scientific and engineering settings, such as biomedical, chemical, and industrial processes involving three or more liquid components. As one of the most popular approaches for modeling interfacial dynamics, the phase-field method provides a state-of-the-art alternative interface capturing approach for multiphase flow problems (see [4,13,16,18,21,27,28] and references therein). Some reasons include its simplicity of formulation and transparent relations of its model parameters to the physical properties. Additionally, the phase-field models and their hydrodynamic extensions are usually derived by following thermodynamic laws, i.e., thermodynamically consistent, making them physically sound. A typical example extensively studied is the Cahn-Hilliard-Navier-Stokes system for simulating the dynamics of multiphase fluid mixtures. This paper mainly focuses on the ternary-component Cahn-Hilliard-Navier-Stokes (ternary-NSCH) system to better illustrate ideas. Notably, our idea also applies to many other hydrodynamic phase-field models.

The three-component Cahn-Hilliard-Navier-Stokes model is generalized from the two-phase scenario [3] by introducing three independent phase-field variables (ϕ_1,ϕ_2,ϕ_3) while these unknowns are linked through the hyperplane relation $\phi_1+\phi_2+\phi_3=1$. Please refer to related papers [2, 3, 10, 19, 22] for more details. Traditionally, a Lagrangian multiplier was adopted into the system that introduced the first coupled nonlinear term among the three-phase variables [20,38]. However, such a simple system is not well-posed for the total spreading case, and some nonphysical instabilities at interfaces may occur [2,3]. To remedy this defect, a sixth-order polynomial-type coupling potential is added to the free energy to ensure the system is well-posed. Developing efficient numerical approximations for solving the three-component Cahn-Hilliard-Navier-Stokes model remains challenging due to the coupling of multi-physical fields with hydrodynamics and their natural nonlinearity.

The phase-field models and their hydrodynamic extensions are usually derived from an energy variational approach, so they naturally admit a free energy dissipation law. This is also known as thermodynamically consistent. When the numerical schemes exploit the variational structure and preserve the dissipation law numerically, they are called energy stable [9]. Suppose such numerical structure-preserving property does not depend on the time step sizes. In that case, the numerical schemes are called ly energy stable. In the past few decades, significant progress in developing structure-preserving algorithms to solve thermodynamical and hydrodynamical phase-field models have been made, for instance, the fully-implicit structure-preserving schemes [3, 33], the convex splitting schemes [5, 8, 41], stabilizer technique [23, 26, 32]. In the past few years, the invariant energy quadratization (IEQ) method and the scalar auxiliary variable (SAV) method, even in combination with stabilization terms, also have fueled the development of energy stable schemes for solving the ternary-component phase-field models [34, 36–38, 42, 43]. However, when some of these methods are applied to solving thermodynamically consistent models, the resulting schemes warrant

a modified energy dissipation law instead of the original energy dissipative law. Truncation errors are introduced during numerical calculations so that the numerical solutions of the auxiliary variables are no longer equivalent to their original continuous definitions. Recently, a Lagrange multiplier method based on the SAV approach presented by Cheng *et al.* [7] and a generalized SAV method proposed by Yang and Dong [40] aimed at further extending the scope of searching strategies for energy stable numerical schemes. The methods have been applied to some fields [12, 39]. More recently, Zhao *et al.* [17, 44] propose one essential relaxation technique to overcome this issue, which highly improves the accuracy and consistency of the IEQ/SAV method. Meanwhile, recent advances include the supplementary variable (SVM) method [11, 15].

Although the ternary-component phase-fluid flow model has been investigated for over a decade, most existing numerical algorithms focus on "dry" phase-field models without flow fields. This is insufficient for many applications for which hydrodynamics is essential. Once performing the coupling between the ternary Cahn-Hilliard and the Navier-Stokes equation for an incompressible flow, it will lead to some highly nonlinear problems. Undoubtedly, this will also pose a noticeable challenge for numerical approximations. To our knowledge, only a few second-order numerical schemes on energy stable for solving the ternary-NSCH model [35, 36] are available in the literature. However, their schemes inherit a modified energy law with auxiliary variables rather than the original energy law. This motivates us to develop efficient numerical approximations that warrant the original physical structure, which we name physics-informed.

We present two efficient numerical methods for solving the ternary-component Cahn-Hilliard-Navier-Stokes model to address these issues. They inherit mass conservation and original energy stability, achieving second-order accuracy. First, we transform the three-variable system into a two-variable one by utilizing the incompressibility condition $\phi_1 + \phi_2 + \phi_3 = 1$. This transformation allows us to solve a problem with two-phase variables, which leads to a notable reduction in computational effort. Second, we reformulate the system using constrained optimization SVM fashion to devise numerical schemes that inherit the original physical structure. Note that the new SVM formulation is equivalent to the original system. This provides a paradigm for developing algorithms that preserve thermodynamically consistent properties. Third, by combining the second-order differentiation formula (BDF2) and implicit-explicit Crank-Nicolson type scheme, we develop two efficient schemes that can possess mass conservation law and original energy stability. We highlight that our proposed BDF2 scheme can be rigorously proven to warrant the original energy law. The proposed schemes involve only constant and time-independent coefficient matrices that can be pre-computed, with a negligible additional cost of solving a scalar nonlinear equation. In the end, several numerical experiments in 2D and 3D space are presented to validate the effectiveness of the current methods.

The outline of this paper is the following. In Section 2, we briefly introduce the three-component Cahn-Hilliard-Navier-Stokes model, revisit its properties of mass conservation and energy dissipation law and reformulate this model into the SVM form with constrained optimization. Then we construct two types of physics-informed structure-preserving numerical schemes that maintain mass conservation and original energy stability. The structure-preserving properties are proved rigorously in Section 3. Fast implementation for the proposed schemes is provided in Section 4. Section 5 presents a series of numerical experiments in 2D and 3D space to show the newly developed schemes' accuracy, efficiency, and usefulness. Finally, some concluding remarks are drawn in Section 6.

2. Thermodynamical consistent hydrodynamic phase field models for ternary incompressible viscous fluid flows

2.1. Model formulation

A general thermodynamically consistent hydrodynamical phase-field model for a three-component fluid flow system was proposed in [3]. Here, we briefly recall the essential ingredients in the multiphase fluid model and discuss its energy dissipation property. Assume that the domain $\Omega \in \mathbb{R}^d$ is smooth, rectangular, open-bounded, and connected, with d=2,3. We define the L^2 inner product of any two functions $f(\mathbf{x})$ and $g(\mathbf{x})$ as follows:

$$(f,g) = \int_{\Omega} f(\mathbf{x})g(\mathbf{x})d\mathbf{x},$$

and the corresponding L^2 norm of $f(\mathbf{x})$ is denoted by $||f|| = (f, f)^{1/2}$.

Consider a three-component fluid flows system in an incompressible viscous fluid matrix governed by the Navier-Stokes equation. The governing system of equations for fluid flow is given by

$$\rho\left(\mathbf{u}_{t} + \frac{1}{2}\left(\mathbf{u} \cdot \nabla \mathbf{u} + \nabla \cdot (\mathbf{u}\mathbf{u})\right)\right) = -\nabla p + \nabla \cdot \boldsymbol{\tau} + \mathbf{F},\tag{2.1}$$

$$\nabla \cdot \mathbf{u} = 0, \tag{2.2}$$

where ρ is the density of the fluid mixture, ${\bf u}$ is the mass-average velocity, ${m au}$ is the viscous stress tensor and ${\bf F}$ is the external force.

We set ϕ_i as the volume fraction of *i*-th component in the fluid mixture. The three volume fractions ϕ_1, ϕ_2, ϕ_3 are linked though the consistency constraint as

$$\phi_1 + \phi_2 + \phi_3 = 1. \tag{2.3}$$

This is the link condition $\phi = (\phi_1, \phi_2, \phi_3)$, where it belongs to be the hyperplane of

$$S = \{ \phi = (\phi_1, \phi_2, \phi_3) \mid \phi_1 + \phi_2 + \phi_3 = 1, \ \phi_i \in [0, 1] \}.$$
 (2.4)

For the three-phase model, the free energy of the mixture [2,3] is given by

$$F^{triph}[\phi] = \frac{3\epsilon^2}{8} \sum_{i=1}^{3} \int_{\Omega} \Sigma_i |\nabla \phi_i|^2 d\mathbf{x} + 12 \int_{\Omega} F(\phi_1, \phi_2, \phi_3) d\mathbf{x},$$
 (2.5)

where Σ_i is called the spreading coefficient [1,2] of the phase i at the interface between phase j and phase k. When $\Sigma_i > 0$, it represents the partial case; if $\Sigma_i < 0$, it is called the total case. To be algebraically consistent with the two-phase system, the three surface tension parameters σ_{12}, σ_{13} and σ_{23} should verify the following conditions:

$$\Sigma_1 = \sigma_{12} + \sigma_{13} - \sigma_{23}, \quad \Sigma_2 = \sigma_{12} + \sigma_{23} - \sigma_{13}, \quad \Sigma_3 = \sigma_{13} + \sigma_{23} - \sigma_{12}.$$
 (2.6)

The nonlinear potential $F(\phi_1, \phi_2, \phi_3)$ reads as

$$F(\phi_1, \phi_2, \phi_3) = \sigma_{12}\phi_1^2\phi_2^2 + \sigma_{23}\phi_2^2\phi_3^2 + \sigma_{13}\phi_1^2\phi_3^2 + \phi_1\phi_2\phi_3(\Sigma_1\phi_1 + \Sigma_2\phi_2 + \Sigma_3\phi_3) + 3\Lambda\phi_1^2\phi_2^2\phi_3^2,$$
(2.7)

where Λ is a non-negative constant. Note that the Λ term is artificial. Some other choices are possible. It is introduced to ensure the free energy has a lower bound in the total spread case. Some detailed discussions can be found in [2]. Due to ϕ_i , i=1,2,3, satisfying the constraint condition (2.3), it implies

$$F(\phi_1, \phi_2, \phi_3) = \frac{\Sigma_1}{2}\phi_1^2(1 - \phi_1)^2 + \frac{\Sigma_2}{2}\phi_2^2(1 - \phi_2)^2 + \frac{\Sigma_3}{2}\phi_3^2(1 - \phi_3)^2 + 3\Lambda\phi_1^2\phi_2^2\phi_3^2.$$
 (2.8)

Lemma 2.1 ([2]). There exists a constant $\underline{\Sigma} > 0$, such that

$$\Sigma_1|x|^2 + \Sigma_2|y|^2 + \Sigma_3|z|^2 \ge \underline{\Sigma}(|x|^2 + |y|^2 + |z|^2),\tag{2.9}$$

where for any x + y + z = 0, if and only if the following condition holds:

$$\Sigma_1 \Sigma_2 + \Sigma_2 \Sigma_3 + \Sigma_1 \Sigma_3 > 0, \quad \Sigma_i + \Sigma_j > 0, \quad \forall i \neq j.$$
 (2.10)

Define the total energy of the three phase fluid-mixture system \mathcal{E} include the kinetic energy E_k and the free energy F^{triph} , namely,

$$\mathcal{E}[\mathbf{u}, \boldsymbol{\phi}] = E_k(\mathbf{u}) + F^{triph}[\boldsymbol{\phi}], \quad E_k(\mathbf{u}) = \int_{\Omega} \frac{\rho}{2} |\mathbf{u}|^2 d\mathbf{x}.$$
 (2.11)

For simplicity, we assume the density and viscosity of each component are constant in this study. We will consider the case where they are different in subsequent studies. The hydrodynamically coupled three-component Cahn-Hilliard phase field model is formulated as

$$\rho\left(\mathbf{u}_{t} + \frac{1}{2}\left(\mathbf{u} \cdot \nabla \mathbf{u} + \nabla \cdot (\mathbf{u}\mathbf{u})\right)\right) = -\nabla p + \eta \Delta \mathbf{u} - \sum_{i=1}^{3} \phi_{i} \nabla \mu_{i},$$
(2.12a)

$$\nabla \cdot \mathbf{u} = 0, \tag{2.12b}$$

$$\partial_t \phi_i + \nabla \cdot (\phi_i \mathbf{u}) = M \Delta \frac{\mu_i}{\Sigma_i}, \quad i = 1, 2, 3,$$
 (2.12c)

$$\mu_i = -\frac{3\epsilon^2}{4} \Sigma_i \Delta \phi_i + 12 \frac{\partial F(\phi_1, \phi_2, \phi_3)}{\partial \phi_i}.$$
 (2.12d)

The boundary conditions are not unique. On the domain boundary $\partial\Omega$, the periodic boundary condition for all variables or the following physical boundary conditions are used:

$$\mathbf{u}(\mathbf{x},t) = 0, \quad \mathbf{n} \cdot \nabla \mu_i(\mathbf{x},t) = 0, \quad \mathbf{n} \cdot \nabla \phi_i(\mathbf{x},t) = 0, \quad (\mathbf{x},t) \in \partial \Omega \times (0,T], \quad (2.13)$$

where n denotes the unit outward normal vector along the boundary. The three-component Cahn-Hilliard-Navier-Stokes system in (2.12a)-(2.12d) with (2.13) follows the second law of thermodynamics in the isothermal case, namely,

$$\frac{\mathrm{d}\mathcal{E}[\mathbf{u}, \boldsymbol{\phi}]}{\mathrm{d}t} = -\eta \|\mathbf{u}\|^2 - M \sum_{i=1}^3 \left(\Sigma_i \left\| \frac{\nabla \mu_i}{\Sigma_i} \right\|^2 \right) \le -\eta \|\mathbf{u}\|^2 - M \underline{\Sigma} \sum_{i=1}^3 \left\| \frac{\nabla \mu_i}{\Sigma_i} \right\|^2, \quad (2.14)$$

where the last inequality is obtained by using Lemma 2.1.

With the aid of the constraint (2.3), the energy (2.11) can be recasted as

$$\mathcal{E}[\mathbf{u}, \phi_1, \phi_3] = E_k[\mathbf{u}] + \frac{3\epsilon^2}{8} \int_{\Omega} \left[\Sigma_1 |\nabla \phi_1|^2 + \Sigma_3 |\nabla \phi_3|^2 + \Sigma_2 |\nabla (\phi_1 + \phi_3)|^2 \right] d\mathbf{x}$$
$$+ 12 \int_{\Omega} F(\phi_1, \phi_3) d\mathbf{x},$$

where $F(\phi_1, \phi_3)$ is given by

$$F(\phi_1, \phi_3) = \frac{\Sigma_1}{2} \phi_1^2 (1 - \phi_1)^2 + \frac{\Sigma_2}{2} (1 - \phi_1 - \phi_3)^2 (\phi_1 + \phi_3)^2 + \frac{\Sigma_3}{2} \phi_3^2 (1 - \phi_3)^2 + 3\Lambda \phi_1^2 \phi_3^2 (1 - \phi_1 - \phi_3)^2.$$

Using the generalized Onsager principle [29], one can rewrite system (2.12a)-(2.12d) as the following equivalent two phase-field variables system:

$$\rho\left(\mathbf{u}_{t} + \frac{1}{2}\left(\mathbf{u} \cdot \nabla \mathbf{u} + \nabla \cdot (\mathbf{u}\mathbf{u})\right)\right) = -\nabla p + \eta \Delta \mathbf{u} - (\phi_{1}\nabla \mu_{1} + \phi_{3}\nabla \mu_{3}), \qquad (2.15a)$$

$$\nabla \cdot \mathbf{u} = 0, \tag{2.15b}$$

$$\partial_t \phi_i + \nabla \cdot (\phi_i \mathbf{u}) = M \Delta \frac{\mu_i}{\Sigma_i}, \quad i = 1, 3,$$
 (2.15c)

$$\mu_1 = -\frac{3\epsilon^2}{4} \Sigma_1 \Delta \phi_1 - \frac{3\epsilon^2}{4} \Sigma_2 (\Delta \phi_1 + \Delta \phi_3) + 12 \frac{\partial F(\phi_1, \phi_3)}{\partial \phi_1}, \tag{2.15d}$$

$$\mu_3 = -\frac{3\epsilon^2}{4} \Sigma_3 \Delta \phi_3 - \frac{3\epsilon^2}{4} \Sigma_2 (\Delta \phi_1 + \Delta \phi_3) + 12 \frac{\partial F(\phi_1, \phi_3)}{\partial \phi_3}.$$
 (2.15e)

By taking the L^2 inner product of (2.15a) with \mathbf{u} , (2.15c) with μ_i , (2.15d) and (2.15e) with $-\partial_t \phi_1$ and $-\partial_t \phi_3$, respectively, and using the integration by parts, then putting the results together, it yields

$$\frac{\mathrm{d}\mathcal{E}[\mathbf{u},\phi_1,\phi_3]}{\mathrm{d}t} = -\eta \|\mathbf{u}\|^2 - M\left(\Sigma_1 \left\|\frac{\nabla \mu_1}{\Sigma_1}\right\|^2 + \Sigma_3 \left\|\frac{\nabla \mu_3}{\Sigma_3}\right\|^2\right) \le 0.$$
 (2.16)

Note that the above inequality also holds for the total spreading scenario under the condition (2.10) since there can be one negative coefficient Σ_i among $\Sigma=(\Sigma_1,\Sigma_2,\Sigma_3)$, that is, $\Sigma_2\leq 0$. Therefore, one can replace the order parameter with respect to the negative coefficient with two others. In this sense, we only need to solve ϕ_1 and ϕ_3 at each time step, and the computation is remarkably simplified.

Remark 2.1. One principle in developing numerical schemes for solving the ternary CHNS system in (2.12a)-(2.12d) or (2.15a)-(2.15d) is to warrant that the numerical solutions also inherit the energy law in (2.14) or (2.16).

2.2. Model reformulation using the supplementary variable method (SVM)

In this subsection, we consider the following extended incompressible equivalent ternary CHNS model, including the deduced energy dissipation equation:

$$\rho\left(\mathbf{u}_{t} + \frac{1}{2}\left(\mathbf{u} \cdot \nabla \mathbf{u} + \nabla \cdot (\mathbf{u}\mathbf{u})\right)\right) = -\nabla p + \eta \Delta \mathbf{u} - (\phi_{1}\nabla \mu_{1} + \phi_{3}\nabla \mu_{3}), \tag{2.17a}$$

$$\nabla \cdot \mathbf{u} = 0, \tag{2.17b}$$

$$\partial_t \phi_i + \nabla \cdot (\phi_i \mathbf{u}) = M \Delta \frac{\mu_i}{\sum_i}, \quad i = 1, 3,$$
 (2.17c)

$$\mu_1 = -\frac{3\epsilon^2}{4} \Sigma_1 \Delta \phi_1 - \frac{3\epsilon^2}{4} \Sigma_2 (\Delta \phi_1 + \Delta \phi_3) + 12 \frac{\partial F(\phi_1, \phi_3)}{\partial \phi_1} + S\Sigma_1 (\phi_1 - \phi_1), \quad (2.17d)$$

$$\mu_{3} = -\frac{3\epsilon^{2}}{4}\Sigma_{3}\Delta\phi_{3} - \frac{3\epsilon^{2}}{4}\Sigma_{2}(\Delta\phi_{1} + \Delta\phi_{3}) + 12\frac{\partial F(\phi_{1}, \phi_{3})}{\partial\phi_{3}} + S\Sigma_{3}(\phi_{3} - \phi_{3}), \quad (2.17e)$$

$$\frac{\mathrm{d}\mathcal{E}}{\mathrm{d}t} = -\eta \|\nabla \mathbf{u}\|^2 - M \left(\Sigma_1 \left\| \frac{\nabla \mu_1}{\Sigma_1} \right\|^2 + \Sigma_3 \left\| \frac{\nabla \mu_3}{\Sigma_3} \right\|^2 \right), \tag{2.17f}$$

where $S \ge 0$ is a stabilizing constant, which is crucial to improving energy stability using relatively large time steps. See the effect of stabilizer in numerical tests.

To aid in devising algorithms that preserve the original energy dissipation law, we first reformulate this model using a novel supplementary variable method. Assuming that we have already obtained the solution of the original system up $t=t_n>0$, we would like to find the solution up to $t_{n+1}>t_n$. To do this, we introduce a time-independent supplementary variable α in $t\in(t_n,t_{n+1})$, and then reformulate the original model into the following constrained optimization problem:

$$\min_{\alpha} |\alpha|^2 \tag{2.18a}$$

s.t.
$$\rho\left(\mathbf{u}_{t} + \frac{1}{2}\left(\mathbf{u} \cdot \nabla \mathbf{u} + \nabla \cdot (\mathbf{u}\mathbf{u})\right)\right) = -\nabla p + \eta \Delta \mathbf{u} - (\phi_{1}\nabla \mu_{1} + \phi_{3}\nabla \mu_{3}) + \alpha \mathbf{g}[\mathbf{u}, \phi_{1}, \phi_{3}],$$
(2.18b)

$$\nabla \cdot \mathbf{u} = 0, \tag{2.18c}$$

$$\partial_t \phi_i + \nabla \cdot (\phi_i \mathbf{u}) = M \Delta \frac{\mu_i}{\Sigma_i} + \alpha(t) h_i[\mathbf{u}, \phi_1, \phi_3], \quad i = 1, 3,$$
(2.18d)

$$\mu_1 = -\frac{3\epsilon^2}{4} \Sigma_1 \Delta \phi_1 - \frac{3\epsilon^2}{4} \Sigma_2 (\Delta \phi_1 + \Delta \phi_3) + 12 \frac{\partial F(\phi_1, \phi_3)}{\partial \phi_1} + S\Sigma_1 (\phi_1 - \phi_1), \quad (2.18e)$$

$$\mu_3 = -\frac{3\epsilon^2}{4}\Sigma_3\Delta\phi_3 - \frac{3\epsilon^2}{4}\Sigma_2(\Delta\phi_1 + \Delta\phi_3) + 12\frac{\partial F(\phi_1, \phi_3)}{\partial\phi_3} + S\Sigma_3(\phi_3 - \phi_3), \quad (2.18f)$$

$$\frac{\mathrm{d}\mathcal{E}}{\mathrm{d}t} = -\eta \|\nabla \mathbf{u}\|^2 - M \left(\Sigma_1 \left\| \frac{\nabla \mu_1}{\Sigma_1} \right\|^2 + \Sigma_3 \left\| \frac{\nabla \mu_3}{\Sigma_3} \right\|^2 \right), \tag{2.18g}$$

where $\mathbf{g}[\mathbf{u},\phi_1,\phi_3]$ and $h_i[\mathbf{u},\phi_1,\phi_3]$ are user-supplied functions and may depend on themselves and their low order spatial derivatives. This seems to be a trivial mathematical statement, given that $\alpha=0$ is a trivial solution to this problem. However, developing numerical schemes for solving this model provides a paradigm for designing algorithms that preserve the original structure.

Remark 2.2. In the SVM, there are many possibilities for choosing \mathbf{g} and h_i . However, to eliminate the pressure p by using $\nabla \cdot \mathbf{u}$ so that our developed algorithm in the paper can be solved efficiently, we choose $\mathbf{g} = \rho \mathbf{u}$. In addition, to ensure the volume conservation of each phase and the incompressibility condition $\phi_1 + \phi_2 + \phi_3 = 1$, we need to pick $h_i = \Delta \mu_i / \Sigma_i$ in this study.

3. Physics-informed structure-preserving schemes with original-energy stability

In the following, we will detail two efficient numerical approximations: using the second-order backward differentiation formula (BDF2) and the implicit-explicit Crank-Nicolson scheme. For ease of presentation, we apply the temporal discretization directly to the constrained optimization problem in (2.18a)-(2.18g).

Let $n \geq 0$ be the time step index, and $(\bullet)^n$ represents the variable (\bullet) at time step t_n , corresponding to the time $t = n\tau$, where τ is the time step size. If a real-valued parameter θ is involved, $(\bullet)^{n+\theta}$ denotes the variable (\bullet) at time step $n + \theta$, corresponding to the time $t = (n + \theta)\tau$. We also introduce the notations

$$\overline{(\bullet)}^{n+1} = 2(\bullet)^n - (\bullet)^{n-1}, \quad \overline{(\bullet)}^{n+\frac{1}{2}} = \frac{3}{2}(\bullet)^n - \frac{1}{2}(\bullet)^{n-1}, \quad (\bullet)^{n+\frac{1}{2}} = \frac{1}{2}((\bullet)^n + (\bullet)^{n+1}). \quad (3.1)$$

The first second-order scheme we developed is based on the BDF2 strategy for this system in (2.18a)-(2.18g). Given $(\mathbf{u}^{n-1}, \phi^{n-1})$ and (\mathbf{u}^n, ϕ^n) , we update $(\mathbf{u}^{n+1}, \phi^{n+1})$ by the following scheme.

Scheme 3.1 (SVM-BDF2). We update $(\mathbf{u}^{n+1}, \phi_i^{n+1})$ via the following two steps:

Step 1. Calculate the predictive solution $(\mathbf{u}_*^{n+1},\phi_{i,*}^{n+1})$

$$\frac{3\phi_{i,*}^{n+1} - 4\phi_i^n + \phi_i^{n-1}}{2\tau} + \nabla \cdot (\overline{\phi}_i^{n+1} \overline{\mathbf{u}}^{n+1}) = M\Delta \frac{\mu_i \left[\phi_{i,*}^{n+1}, \overline{\phi}_1^{n+1}, \overline{\phi}_3^{n+1}\right]}{\Sigma_i}, \quad i = 1, 3, \quad (3.2a)$$

$$\mu_{i} \left[\phi_{i,*}^{n+1}, \overline{\phi}_{1}^{n+1}, \overline{\phi}_{3}^{n+1} \right]$$

$$= -\frac{3\epsilon^{2}}{4} \Sigma_{i} \Delta \phi_{i,*}^{n+1} + 12 \frac{\partial F(\overline{\phi}_{1}^{n+1}, \overline{\phi}_{3}^{n+1})}{\partial \phi_{i}} + S \Sigma_{i} \left(\phi_{i,*}^{n+1} - \overline{\phi}_{i}^{n+1} \right),$$

$$\rho \left(\frac{3\mathbf{u}_{*}^{n+1} - 4\mathbf{u}^{n} + \mathbf{u}^{n-1}}{2\tau} + B(\overline{\mathbf{u}}^{n+1}, \overline{\mathbf{u}}^{n+1}) \right)$$

$$= -\nabla p^{n+1} + \eta \Delta \mathbf{u}_{*}^{n+1} - \left(\phi_{1,*}^{n+1} \nabla \mu_{1,*}^{n+1} + \phi_{3,*}^{n+1} \nabla \mu_{3,*}^{n+1} \right),$$
(3.2c)

$$\nabla \cdot \mathbf{u}_*^{n+1} = 0, \tag{3.2d}$$

where $B(\mathbf{u}, \mathbf{v}) = (\mathbf{u} \cdot \nabla \mathbf{v} + \nabla \cdot (\mathbf{u}\mathbf{v}))/2$ and $\mu_{i*}^{n+1} = \mu[\phi_{i*}^{n+1}, \phi_{1*}^{n+1}, \phi_{3*}^{n+1}].$

Step 2. Update $(\mathbf{u}^{n+1}, \phi_i^{n+1})$ via solving the following constrained optimization problem:

$$\min_{\alpha^{n+1}} (\alpha^{n+1})^{2}, \qquad (3.3a)$$
s.t.
$$\frac{1}{2\tau} (3\phi_{i}^{n+1} - 4\phi_{i}^{n} + \phi_{i}^{n-1}) + \nabla \cdot (\phi_{i,*}^{n+1} \mathbf{u}_{*}^{n+1})$$

$$= M\Delta \frac{\mu_{i} [\phi_{i}^{n+1}, \phi_{1,*}^{n+1}, \phi_{3,*}^{n+1}]}{\Sigma_{i}} + \alpha^{n+1} h_{i}^{n+1,*}, \qquad (3.3b)$$

$$\mu_{i} [\phi_{i}^{n+1}, \phi_{1,*}^{n+1}, \phi_{3,*}^{n+1}]$$

$$= -\frac{3\epsilon^{2}}{4} \Sigma_{i} \Delta \phi_{i}^{n+1} + 12 \frac{\partial F(\phi_{1,*}^{n+1}, \phi_{3,*}^{n+1})}{\partial \phi_{i}} + S\Sigma_{i} (\phi_{i}^{n+1} - \phi_{i,*}^{n+1}), \qquad (3.3c)$$

$$\rho \left(\frac{3\mathbf{u}^{n+1} - 4\mathbf{u}^{n} + \mathbf{u}^{n-1}}{2\tau} + B(\mathbf{u}_{*}^{n+1}, \mathbf{u}_{*}^{n+1}) \right)$$

$$= -\nabla p^{n+1} + \eta \Delta \mathbf{u}^{n+1} - (\phi_{1,*}^{n+1} \nabla \mu_{1,*}^{n+1} + \phi_{3,*}^{n+1} \nabla \mu_{3,*}^{n+1}) + \alpha^{n+1} \mathbf{g}^{n+1,*}, \qquad (3.3d)$$

$$\nabla \cdot \mathbf{u}^{n+1} = 0, \qquad (3.3e)$$

$$\frac{1}{2\tau} (3\mathcal{E}^{n+1} - 4\mathcal{E}^{n} + \mathcal{E}^{n-1})$$

$$= -\eta \|\nabla \mathbf{u}_{*}^{n+1}\|^{2} - M\left(\Sigma_{1} \left\| \frac{\nabla \mu_{1,*}^{n+1}}{\Sigma_{1}} \right\|^{2} + \Sigma_{3} \left\| \frac{\nabla \mu_{3,*}^{n+1}}{\Sigma_{3}} \right\|^{2}\right). \qquad (3.3f)$$

Remark 3.1. The SVM-BDF2 scheme needs the information at (n-1)-th and n-th time steps. To initiate the second-order schemes in the numerical experiments, we need the values of (\mathbf{u}^1, ϕ^1) that can be computed by the following first-order accurate scheme with two steps:

Step 1. Calculate the predictive solution $(\mathbf{u}_*^1, \phi_{i,*}^1)$

$$\frac{\phi_{i,*}^1 - \phi_i^0}{\tau} + \nabla \cdot \left(\phi_i^0 \mathbf{u}^0\right) = M \Delta \frac{\mu_i \left[\phi_{i,*}^1, \phi_1^0, \phi_3^0\right]}{\Sigma_i}, \quad i = 1, 3,$$

$$\mu_{i} \left[\phi_{i,*}^{1}, \phi_{1}^{0}, \phi_{3}^{0} \right] = -\frac{3\epsilon^{2}}{4} \Sigma_{i} \Delta \phi_{i,*}^{1} + 12 \frac{\partial F \left(\phi_{1}^{0}, \phi_{3}^{0} \right)}{\partial \phi_{i}} + S \Sigma_{i} \left(\phi_{i,*}^{1} - \phi_{i}^{0} \right),$$

$$\rho \left(\frac{\mathbf{u}_{*}^{1} - \mathbf{u}^{0}}{\tau} + B(\mathbf{u}^{0}, \mathbf{u}^{0}) \right) = -\nabla p^{1} + \eta \Delta \mathbf{u}_{*}^{1} - \left(\phi_{1,*}^{1} \nabla \mu_{1,*}^{1} + \phi_{3,*}^{1} \nabla \mu_{3,*}^{1} \right),$$

$$\nabla \cdot \mathbf{u}_{*}^{1} = 0,$$

where $\mu_{i,*}^1 = \mu[\phi_{i,*}^1, \phi_{1,*}^1, \phi_{3,*}^1]$.

Step 2. Update (\mathbf{u}^1,ϕ_i^1) via solving the following constrained optimization problem:

$$\min_{\alpha^1} (\alpha^1)^2$$
,

$$\begin{aligned} \text{s.t.} \quad & \frac{\phi_i^1 - \phi_i^0}{\tau} + \nabla \cdot \left(\phi_{i,*}^1 \mathbf{u}_*^1\right) = M \Delta \frac{\mu_i \left[\phi_i^1, \phi_{1,*}^1, \phi_{3,*}^1\right]}{\Sigma_i} + \alpha^1 h_i^{1,*}, \\ & \mu_i \left[\phi_i^1, \phi_{1,*}^1, \phi_{3,*}^1\right] = -\frac{3\epsilon^2}{4} \Sigma_i \Delta \phi_i^1 + 12 \frac{\partial F(\phi_{1,*}^1, \phi_{3,*}^1)}{\partial \phi_i} + S \Sigma_i \left(\phi_i^1 - \phi_{i,*}^1\right), \\ & \rho \left(\frac{\mathbf{u}^1 - \mathbf{u}^0}{\tau} + B \left(\mathbf{u}_*^1, \mathbf{u}_*^1\right)\right) = -\nabla p^1 + \eta \Delta \mathbf{u}^1 - \left(\phi_{1,*}^1 \nabla \mu_{1,*}^1 + \phi_{3,*}^1 \nabla \mu_{3,*}^1\right) + \alpha^1 \mathbf{g}^{1,*}, \\ & \nabla \cdot \mathbf{u}^1 = 0, \\ & \frac{\mathcal{E}^1 - \mathcal{E}^0}{\tau} = -\eta \|\nabla \mathbf{u}_*^1\|^2 - M \left(\Sigma_1 \left\|\frac{\nabla \mu_{1,*}^1}{\Sigma_1}\right\|^2 + \Sigma_3 \left\|\frac{\nabla \mu_{3,*}^1}{\Sigma_3}\right\|^2\right). \end{aligned}$$

It is worth noting that the efficient implementation skill in the next section can be straightforwardly adopted for the above first-order accurate scheme.

The time marching scheme SVM-BDF2 has the following properties.

Theorem 3.1. Scheme 3.1 is mass conservative for each phase, i.e.,

$$(\phi_i^{n+1}, 1) = (\phi_i^n, 1), \quad i = 1, 2, 3, \quad \forall n \ge 0.$$
 (3.6)

Proof. Integrating Eq. (3.3b) over Ω , thanks to $\phi_2^n=1-\phi_1^n-\phi_3^n$, for any n, $(h_i^{n+1},1)=0$ and the integration by parts, it yields the mass conservation for each phase.

Theorem 3.2. Assume $\mathcal{E}^1 \leq \mathcal{E}^0$. Scheme 3.1 is energy stable in the sense that

$$\mathcal{E}^{n+1} \le \mathcal{E}^n,\tag{3.7}$$

where the original energy \mathcal{E}^n is given by

$$\mathcal{E}^{n} = \frac{\rho}{2} \|\mathbf{u}^{n}\|^{2} + \frac{3\epsilon^{2}}{8} (\Sigma_{1} \|\nabla\phi_{1}^{n}\|^{2} + \Sigma_{3} |\nabla\phi_{3}^{n}|^{2} + \Sigma_{2} |\nabla\phi_{1}^{n} + \nabla\phi_{3}^{n}|^{2}) + 12(F(\phi_{1}^{n}, \phi_{3}^{n}), 1).$$
(3.8)

Proof. By Lemma 2.1 and (3.3f), one can easily obtain

$$\frac{1}{2\tau} (3\mathcal{E}^{n+1} - 4\mathcal{E}^n + \mathcal{E}^{n-1})$$

$$= -\eta \|\nabla \mathbf{u}_*^{n+1}\|^2 - M \left(\Sigma_1 \left\| \frac{\nabla \mu_{1,*}^{n+1}}{\Sigma_1} \right\|^2 + \Sigma_3 \left\| \frac{\nabla \mu_{3,*}^{n+1}}{\Sigma_3} \right\|^2 \right) \le 0.$$
(3.9)

Thus, one can get

$$\frac{1}{2}(3\mathcal{E}^{n+1} - 4\mathcal{E}^n + \mathcal{E}^{n-1}) = \frac{1}{2}(3(\mathcal{E}^{n+1} - \mathcal{E}^n) - (\mathcal{E}^n - \mathcal{E}^{n-1})) \le 0,$$
(3.10)

which implies

$$\mathcal{E}^{n+1} - \mathcal{E}^n \le \frac{1}{3} (\mathcal{E}^n - \mathcal{E}^{n-1}). \tag{3.11}$$

By the mathematical recursion and $\mathcal{E}^1 \leq \mathcal{E}^0$, it yields

$$\mathcal{E}^{n+1} \le \mathcal{E}^n, \quad \forall \, n. \tag{3.12}$$

The proof is complete.

Remark 3.2. Recently, [7] proposed a new Lagrange multiplier approach to design original energy stable for gradient flows in which its strategy based on BDF2 also only preserves modified energy rather than the original energy. However, our proposed scheme based on BDF2 can maintain the original energy law.

Remark 3.3. For the developed second-order time-marching scheme, the explicit treatments for the nonlinear term and high-order spatial derivatives generally break the stability of the numerical solution. So far, there is no theoretical analysis method to determine it, and the value of the stabilization parameter is generally empirical. Meanwhile, we carefully choose the value of S to avoid introducing large numerical errors to balance the stability and accuracy.

Then if we use the implicit-explicit Crank-Nicolson time-marching scheme, it yields another second-order scheme.

Scheme 3.2 (SVM-CN). Given $(\mathbf{u}^{n-1}, \phi_i^{n-1})$ and (\mathbf{u}^n, ϕ_i^n) , we compute $(\mathbf{u}^{n+1}, \phi_i^{n+1})$ via the following two steps:

Step 1. We solve $(\mathbf{u}^{n+1}_*,\phi^{n+1}_{i,*})$ via the following system:

$$\frac{\phi_{i,*}^{n+1} - \phi_i^n}{\tau} + \nabla \cdot (\overline{\phi}_i^{n+\frac{1}{2}} \overline{\mathbf{u}}^{n+\frac{1}{2}}) = M \Delta \frac{\mu_i \left[\phi_{i,*}^{n+\frac{1}{2}}, \overline{\phi}_1^{n+\frac{1}{2}}, \overline{\phi}_3^{n+\frac{1}{2}} \right]}{\Sigma_i}, \tag{3.13a}$$

$$\mu_{i} \left[\phi_{i,*}^{n+\frac{1}{2}}, \overline{\phi}_{1}^{n+\frac{1}{2}}, \overline{\phi}_{3}^{n+\frac{1}{2}} \right] = -\frac{3\epsilon^{2}}{4} \Sigma_{i} \Delta \phi_{i,*}^{n+\frac{1}{2}} + 12 \frac{\partial F\left(\overline{\phi}_{1}^{n+\frac{1}{2}}, \overline{\phi}_{3}^{n+\frac{1}{2}}\right)}{\partial \phi_{i}} + S \Sigma_{i} \left(\phi_{i,*}^{n+\frac{1}{2}} - \overline{\phi}_{i}^{n+\frac{1}{2}} \right), \tag{3.13b}$$

$$\rho\left(\frac{\mathbf{u}_{*}^{n+1} - \mathbf{u}^{n}}{\tau} + B(\overline{\mathbf{u}}^{n+\frac{1}{2}}, \overline{\mathbf{u}}^{n+\frac{1}{2}})\right)$$

$$= -\nabla p^{n+\frac{1}{2}} + \eta \Delta \mathbf{u}_{*}^{n+\frac{1}{2}} - \left(\phi_{1,*}^{n+\frac{1}{2}} \nabla \mu_{1,*}^{n+\frac{1}{2}} + \phi_{3,*}^{n+\frac{1}{2}} \nabla \mu_{3,*}^{n+\frac{1}{2}}\right), \tag{3.13c}$$

$$\nabla \cdot \mathbf{u}_{*}^{n+\frac{1}{2}} = 0, \tag{3.13d}$$

where

$$B(\mathbf{u}, \mathbf{v}) = \frac{1}{2} (\mathbf{u} \cdot \nabla \mathbf{v} + \nabla \cdot (\mathbf{u} \mathbf{v})), \quad \mu_{i,*}^{n+1} = \mu \left[\phi_{i,*}^{n+1}, \phi_{1,*}^{n+1}, \phi_{3,*}^{n+1} \right], \quad (\bullet)_{*}^{n+\frac{1}{2}} = \frac{1}{2} \left((\bullet)_{*}^{n+1} + (\bullet)^{n} \right).$$

Step 2. Update $(\mathbf{u}^{n+1}, \phi_i^{n+1})$ via

$$\min_{\alpha^{n+\frac{1}{2}}} \ (\alpha^{n+\frac{1}{2}})^2, \tag{3.14a}$$

s.t.
$$\frac{\phi_{i}^{n+1} - \phi_{i}^{n}}{\tau} + \nabla \cdot \left(\phi_{i,*}^{n+\frac{1}{2}} \mathbf{u}_{*}^{n+\frac{1}{2}}\right) = M\Delta \frac{\mu_{i} \left[\phi_{i}^{n+\frac{1}{2}}, \phi_{1,*}^{n+\frac{1}{2}}, \phi_{3,*}^{n+\frac{1}{2}}\right]}{\Sigma_{i}} + \alpha^{n+\frac{1}{2}} h_{i}^{n+\frac{1}{2},*}, \quad (3.14b)$$

$$\mu_{i} \left[\phi_{i}^{n+\frac{1}{2}}, \phi_{1,*}^{n+\frac{1}{2}}, \phi_{3,*}^{n+\frac{1}{2}}\right]$$

$$= -\frac{3\epsilon^{2}}{4} \Sigma_{i} \Delta \phi_{i}^{n+\frac{1}{2}} + 12 \frac{\partial F\left(\phi_{1,*}^{n+\frac{1}{2}}, \phi_{3,*}^{n+\frac{1}{2}}\right)}{\partial \phi_{i}} + S \Sigma_{i} \left(\phi_{i}^{n+\frac{1}{2}} - \phi_{i,*}^{n+\frac{1}{2}}\right),$$

$$\rho\left(\frac{\mathbf{u}^{n+1} - \mathbf{u}^{n}}{\sigma} + B\left(\mathbf{u}_{*}^{n+\frac{1}{2}}, \mathbf{u}_{*}^{n+\frac{1}{2}}\right)\right)$$
(3.14c)

$$= -\nabla p^{n+\frac{1}{2}} + \eta \Delta \mathbf{u}^{n+\frac{1}{2}} - \left(\phi_{1,*}^{n+\frac{1}{2}} \nabla \mu_{1,*}^{n+\frac{1}{2}} + \phi_{3,*}^{n+\frac{1}{2}} \nabla \mu_{3,*}^{n+\frac{1}{2}}\right) + \alpha^{n+\frac{1}{2}} \mathbf{g}^{n+\frac{1}{2},*}, \quad (3.14d)$$

$$\nabla \cdot \mathbf{u}^{n+\frac{1}{2}} = 0, \tag{3.14e}$$

$$\frac{\mathcal{E}^{n+1} - \mathcal{E}^n}{\tau} = -\eta \left\| \nabla \mathbf{u}_*^{n+\frac{1}{2}} \right\|^2 - M \left(\Sigma_1 \left\| \frac{\nabla \mu_{1,*}^{n+\frac{1}{2}}}{\Sigma_1} \right\|^2 + \Sigma_3 \left\| \frac{\nabla \mu_{3,*}^{n+\frac{1}{2}}}{\Sigma_3} \right\|^2 \right). \tag{3.14f}$$

Theorem 3.3. The Scheme 3.2 preserves the mass conservation for each phase, namely

$$(\phi_i^{n+1}, 1) = (\phi_i^n, 1), \quad i = 1, 2, 3, \quad \forall \ n \ge 0.$$
 (3.15)

Proof. The proof is similar to Theorem 3.1. Thus we leave the details to the interested readers. \Box

Theorem 3.4. The Scheme 3.2 is energy stable.

Proof. The statement is obvious by (3.14f) and completes the proof.

Remark 3.4. Notably, the current schemes in this study based on the SVM approach with constrained optimization are accurate and efficient, and the idea can be readily extended to a broader class of multiphase hydrodynamic models for developing structure-preserving numerical schemes. Although only the time discretization on the semi-discrete schemes is presented in this paper, the fully discrete scheme can be easily derived by combining the proposed semi-discrete scheme in time and finite difference discretization that satisfies summation by parts formulae [6, 25, 30, 31].

4. Efficient implementation strategy

This section will discuss the efficient numerical implementation of our newly proposed schemes. For convenience, we take Scheme 3.1 under the periodic boundary condition and in 2D space as an example to elaborate a fast solver. It follows from (3.2a)-(3.2d) that

$$\mathcal{A}_{11}\phi_{1*}^{n+1} + \mathcal{A}_{12}\phi_{3*}^{n+1} = G_1(\phi_1^{n-1}, \phi_1^n, \overline{\phi}_1^{n+1}, \overline{\phi}_3^{n+1}, \overline{\mathbf{u}}^{n+1}), \tag{4.1}$$

$$\mathcal{A}_{21}\phi_{1,*}^{n+1} + \mathcal{A}_{22}\phi_{3,*}^{n+1} = G_3(\phi_3^{n-1}, \phi_3^n, \overline{\phi}_1^{n+1}, \overline{\phi}_3^{n+1}, \overline{\mathbf{u}}^{n+1}), \tag{4.2}$$

$$\mathcal{B}\mathbf{u}_{*}^{n+1} = \rho \frac{4\mathbf{u}^{n} - \mathbf{u}^{n-1}}{2\tau} - \rho B(\overline{\mathbf{u}}^{n+1}, \overline{\mathbf{u}}^{n+1}) - \nabla p^{n+1} - \phi_{1,*}^{n+1} \nabla \mu_{1,*}^{n+1} - \phi_{3,*}^{n+1} \nabla \mu_{3,*}^{n+1},$$
(4.3)

where $\mathcal{B} = 3\rho/2 - \tau \eta \Delta$ and

$$G_{1}\left(\phi_{1}^{n-1},\phi_{1}^{n},\overline{\phi_{1}}^{n+1},\overline{\phi_{3}}^{n+1},\overline{\mathbf{u}}^{n+1}\right)$$

$$=\frac{4\phi_{1}^{n}-\phi_{1}^{n-1}}{2}+\frac{12\tau M\Delta}{\Sigma_{1}}\left[\frac{\partial F\left(\overline{\phi_{1}}^{n+1},\overline{\phi_{3}}^{n+1}\right)}{\partial\phi_{1}}-S\overline{\phi_{1}}^{n+1}\right]-\tau\nabla\cdot\left(\overline{\phi_{1}}^{n+1}\overline{\mathbf{u}}^{n+1}\right),$$

$$G_{3}\left(\phi_{3}^{n-1},\phi_{3}^{n},\overline{\phi_{1}}^{n+1},\overline{\phi_{3}}^{n+1},\overline{\mathbf{u}}^{n+1}\right)$$

$$=\frac{4\phi_{3}^{n}-\phi_{3}^{n-1}}{2}+\frac{12\tau M\Delta}{\Sigma_{3}}\left[\frac{\partial F\left(\overline{\phi_{1}}^{n+1},\overline{\phi_{3}}^{n+1}\right)}{\partial\phi_{3}}-S\overline{\phi_{3}}^{n+1}\right]-\tau\nabla\cdot\left(\overline{\phi_{3}}^{n+1}\overline{\mathbf{u}}^{n+1}\right),$$

$$\mathcal{A}_{11}=\frac{3}{2}+\frac{3\tau\epsilon^{2}}{4}\frac{\Sigma_{1}+\Sigma_{2}}{\Sigma_{1}}M\Delta^{2}-\tau SM\Delta,\quad \mathcal{A}_{12}=\frac{3\tau\epsilon^{2}}{4}\frac{\Sigma_{2}}{\Sigma_{1}}M\Delta^{2},$$

$$\mathcal{A}_{22}=\frac{3}{2}+\frac{3\tau\epsilon^{2}}{4}\frac{\Sigma_{2}+\Sigma_{3}}{\Sigma_{2}}M\Delta^{2}-\tau SM\Delta,\quad \mathcal{A}_{21}=\frac{3\tau\epsilon^{2}}{4}\frac{\Sigma_{2}}{\Sigma_{2}}M\Delta^{2}.$$

Although $\phi_{1,*}$ and $\phi_{3,*}$ are coupled in (4.1) and (4.2), this system can be transformed into a 2×2 algebraic equation with respect to $\phi_{1,*}$ and $\phi_{3,*}$ for a fixed spatial point (x_j, y_k) by using the diagonalization of a matrix and fast Fourier transform strategies, which can be solved efficiently. For more details on the efficient solution of the coupled system, please refer to [14]. It is a remarkable fact that p^{n+1} can be firstly computed by $\nabla \cdot \mathbf{u}_*^{n+1}$ and then update \mathbf{u}_*^{n+1} via the Eq. (4.3).

Denote

$$\Phi_1^{n+1} = \mathcal{C}_{11}G_1(\phi_1^{n-1}, \phi_1^n \phi_{1,*}^{n+1}, \phi_{3,*}^{n+1}, \mathbf{u}_*^{n+1}) + \mathcal{C}_{12}G_3(\phi_3^{n-1}, \phi_3^n, \phi_{1,*}^{n+1}, \phi_{3,*}^{n+1}, \mathbf{u}_*^{n+1}), \quad (4.4)$$

$$\Phi_3^{n+1} = \mathcal{C}_{21}G_1(\phi_1^{n-1}, \phi_1^n, \phi_{1,*}^{n+1}, \phi_{3,*}^{n+1}, \mathbf{u}_*^{n+1}) + \mathcal{C}_{22}G_3(\phi_3^{n-1}, \phi_3^n, \phi_{1,*}^{n+1}, \phi_{3,*}^{n+1}, \mathbf{u}_*^{n+1}),$$
(4.5)

$$\mathbf{U}^{n+1} = \mathcal{B}^{-1} \left(\rho \frac{4\mathbf{u}^n - \mathbf{u}^{n-1}}{2\tau} - \rho B(\mathbf{u}_*^{n+1}, \mathbf{u}_*^{n+1}) - \nabla p^{n+1} - \phi_{1,*}^{n+1} \nabla \mu_{1,*}^{n+1} - \phi_{3,*}^{n+1} \nabla \mu_{3,*}^{n+1} \right), \quad (4.6)$$

$$\chi_1^n = \mathcal{C}_{11}h_1^{n+1,*} + \mathcal{C}_{12}h_3^{n+1,*}, \quad \chi_3^n = \mathcal{C}_{21}h_1^{n+1,*} + \mathcal{C}_{22}h_3^{n+1,*}, \quad \boldsymbol{\omega}^n = \mathcal{B}^{-1}\mathbf{g}^{n+1,*}, \quad (4.7)$$

where \mathcal{B}^{-1} and \mathcal{A}^{-1} denote the inverse of the operator \mathcal{B} and \mathcal{A} , respectively, which are given by

$$\mathcal{A}^{-1} = \begin{bmatrix} \mathcal{C}_{11} & \mathcal{C}_{12} \\ \mathcal{C}_{21} & \mathcal{C}_{22} \end{bmatrix}, \quad \mathcal{A} = \begin{bmatrix} \mathcal{A}_{11} & \mathcal{A}_{12} \\ \mathcal{A}_{21} & \mathcal{A}_{22} \end{bmatrix}. \tag{4.8}$$

From (3.3b)-(3.3e), it is easily to derive that

$$\phi_i^{n+1} = \Phi_i^{n+1} + \beta^{n+1} \chi_i^n, \quad i = 1, 3,$$

$$\mathbf{u}^{n+1} = \mathbf{U}^{n+1} + \beta^{n+1} \boldsymbol{\omega}^n.$$
(4.9)

in which $\beta^{n+1} = \tau \alpha^{n+1}$ will be determined below. Then plugging (4.9) into (3.3f) yields the following scalar nonlinear algebraic equation:

$$\mathcal{N}(\beta^{n+1}) := 3\mathcal{E} \left[\mathbf{U}^{n+1} + \beta^{n+1} \boldsymbol{\omega}^{n}, \Phi_{i}^{n+1} + \beta^{n+1} \chi_{i}^{n} \right] - 4\mathcal{E}^{n} + \mathcal{E}^{n-1} + 2\tau \eta \left\| \nabla \mathbf{u}_{*}^{n+1} \right\|^{2} + 2\tau M \left(\Sigma_{1} \left\| \frac{\nabla \mu_{1,*}^{n+\frac{1}{2}}}{\Sigma_{1}} \right\|^{2} + \Sigma_{3} \left\| \frac{\nabla \mu_{3,*}^{n+\frac{1}{2}}}{\Sigma_{3}} \right\|^{2} \right).$$

$$(4.10)$$

Consequently, the original optimization problem (3.3a)-(3.3f) can be equivalently transform into

$$\min_{\beta^{n+1}} \quad (\beta^{n+1})^2,$$
 s.t.
$$\mathcal{N}(\beta^{n+1}) = 0.$$
 (4.11)

A standard approach is to introduce Lagrange multiplier λ and consider the Lagrange function as follows:

$$\mathcal{L}(\beta^{n+1}, \lambda) = (\beta^{n+1})^2 - \lambda N(\beta^{n+1}). \tag{4.12}$$

The KKT condition of the constrained optimization problem (4.11) is given by

$$\frac{\partial \mathcal{L}}{\partial \beta^{n+1}} = 2\beta^{n+1} - \lambda \frac{\partial \mathcal{N}(\beta^{n+1})}{\partial \beta^{n+1}} = 0, \tag{4.13}$$

$$\frac{\partial \mathcal{L}}{\partial \beta^{n+1}} = -\mathcal{N}(\beta^{n+1}) = 0. \tag{4.14}$$

To determine (β^{n+1}, λ) , we have to solve the scalar nonlinear equation above by applying certain efficient optimization methods and leave this for future study. We point

out that here we employ Newton's method to solve it with (0,0) as an initial value, where the evaluations of $\partial N/\partial \beta$ and $\partial^2 N/\partial \beta^2$ are also needed. Since the scalar nonlinear algebraic equation $N(\beta^{n+1})$ only depends on the unary polynomial of β^{n+1} and the coefficients of the polynomial can be pre-computed at each time step, which implies the coefficients of $\partial N/\partial \beta$ and $\partial^2 N/\partial \beta^2$ can also be pre-computed. Thus, the cost of this computation is minimal compared to the total cost within a time step because this equation (4.13)-(4.14) is about a scalar number but not a field function. Once β^{n+1} is known, then \mathbf{u}^{n+1} and ϕ_i^{n+1} , i=1,2,3, can be updated respectively via using (4.9). Following the work of [11], the existence of the solution β is guaranteed by the conditions of the following theorem.

Theorem 4.1. Assume that

$$\left(\frac{\delta \mathcal{E}}{\delta \mathbf{u}}[\mathbf{u}^n], g[\mathbf{u}^n]\right) + \left(\frac{\delta \mathcal{E}}{\delta \phi_1} \left[\phi_1^n\right], h_1\left[\phi_1^n\right]\right) + \left(\frac{\delta \mathcal{E}}{\delta \phi_3} \left[\phi_3^n\right], h_3\left[\phi_3^n\right]\right) \neq 0,$$

there exist a $\tau^* > 0$, such that (4.13) and (4.14) define a unique function $\beta = \beta(\tau)$ for all $\tau \in [0, \tau^*]$.

Proof. For τ , β , and λ in a neighborhood of (0,0,0), we define the two following real functions:

$$P(\tau, \beta, \lambda) = 2\beta - \lambda \frac{\partial N}{\partial \beta}, \quad Q(\tau, \beta, \lambda) = -N(\beta).$$
 (4.15)

Combining (4.4)-(4.7) and (4.9), it yields

$$P(0,0,0) = 0, \quad Q(0,0,0) = 0,$$

$$\frac{\partial(P,Q)}{\partial(\beta,\lambda)}\Big|_{(0,0,0)} = \left(\frac{\delta\mathcal{E}}{\delta\mathbf{u}}[\mathbf{u}^n], g[\mathbf{u}^n]\right) + \left(\frac{\delta\mathcal{E}}{\delta\phi_1}[\phi_1^n], h_1[\phi_1^n]\right)$$

$$+ \left(\frac{\delta\mathcal{E}}{\delta\phi_3}[\phi_3^n], h_3[\phi_3^n]\right) \neq 0.$$
(4.16)

Therefore, by using the implicit function theorem for multivariate functions, there exists a $\tau^* > 0$ such that the following system:

$$P(\tau, \beta, \lambda) = 0,$$

$$Q(\tau, \beta, \lambda) = 0$$

define a set of unique smooth functions $\beta := \beta(\tau)$ and $\lambda := \lambda(\tau)$ satisfy

$$P\big(\tau,\beta(\tau),\lambda(\tau)\big)=0,\quad Q\big(\tau,\beta(\tau),\lambda(\tau)\big)=0$$

for all $\tau \in [0, \tau^*]$. The conclusion follows, and the proof is complete.

5. Numerical results and discussion

In this section, we first conduct time-step refinement to test the temporal accuracy of our newly developed schemes. Then we present several numerical simulations to demonstrate the schemes' efficiency and structure-preserving properties. Here, if not explicitly stated, we mainly consider the ternary phase-field hydrodynamic model with periodic boundary conditions. Also, due to the BDF2 and Crank-Nicolson schemes being both second-order accurate, we specifically present the numerical performances of SVM-BDF2 in most scenarios.

Example 5.1 (Accuracy tests). As a first numerical test, we conduct a mesh-refinement study to verify that the developed schemes are second-order in time. The initial conditions are given by

$$\mathbf{u}^{0} = (0,0)^{T},$$

$$\phi_{1}^{0} = \frac{1}{2} \left(1 + \tanh\left(\frac{0.15 - \sqrt{(x - 0.5)^{2} + (y - 0.5)^{2}}}{\epsilon}\right) \right),$$

$$\phi_{3}^{0} = \frac{1}{2} \left(1 - \phi_{1}^{0} \right) \left(1 + \tanh\left(\frac{y - 0.5}{\epsilon}\right) \right),$$

$$\phi_{2}^{0} = 1 - \phi_{1}^{0} - \phi_{3}^{0}.$$
(5.1)

Consider the computational domain $\Omega=[0,1]\times[0,1]$ with 128×128 spatial meshes and we choose the model parameters $M=10^{-5},\epsilon=0.025,\rho=\eta=1,\Lambda=7$ and $S=1/\epsilon$. Since the exact solutions are unknown, we compute the errors by adjacent time steps. In Fig. 1, we list the discrete L^2 and L^∞ errors for variables $\mathbf{u}=(u,v)$ and $\phi=(\phi_1,\phi_2,\phi_3)$ at the end time T=0.1 by taking a linear refinement path $\tau=0.001/2^k,\ k=0,1,2,3,4,5,6$. The numerical results in Fig. 1 indicate that the developed schemes indeed have second-order temporal accuracy in time for all variables, where SVM-BDF2 and SVM-CN are performed. Moreover, one can find that the SVM-CN scheme is slightly more accurate than SVM-BDF2, although both of them are second-order accurate. This may be because the former is an energy-dissipation-rate preserving scheme.

In addition, Fig. 2 shows that the second-order accuracy of the supplementary variable α is reached for the corresponding SVM-BDF2 and SVM-CN schemes. Therefore, these numerical performances from Example 5.1 validate the correctness of our proposed schemes.

Example 5.2 (Numerical comparisons). To show the advantages of our proposed scheme, we conduct some numerical comparisons with the IEQ-BDF2 and fully implicit BDF2 schemes. The initial conditions for phase variables are specified as

$$\phi_1^0 = \frac{1}{2} + \frac{1}{2} \tanh \frac{0.25 - \sqrt{(x - 1.27)^2 + (y - 1.0)^2}}{\epsilon},$$

$$\phi_3^0 = \frac{1}{2} + \frac{1}{2} \tanh \frac{0.25 - \sqrt{(x - 0.73)^2 + (y - 1.0)^2}}{\epsilon},$$

and $\phi_2^0 = 1 - \phi_1^0 - \phi_3^0$. The initial velocity is set as zero.

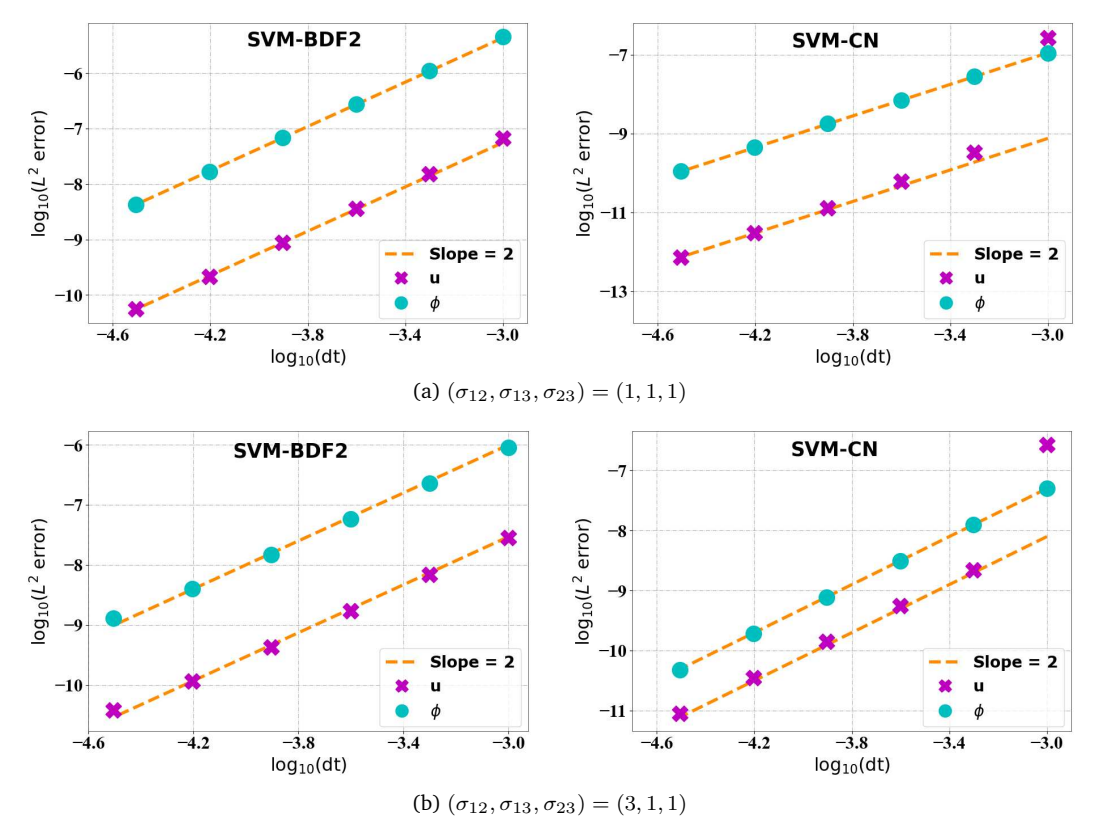


Figure 1: Mesh refinement test of time accuracy for the variables $\mathbf{u}=(u,v)^T$ and $\boldsymbol{\phi}=(\phi_1,\phi_2,\phi_3)^T$, where the surface tension parameters (a): $(\sigma_{12},\sigma_{13},\sigma_{23})=(1,1,1)$ and (b): $(\sigma_{12},\sigma_{13},\sigma_{23})=(3,1,1)$. This illustrates the SVM-BDF2 and SVM-CN schemes can reach their expected second-order accuracy.

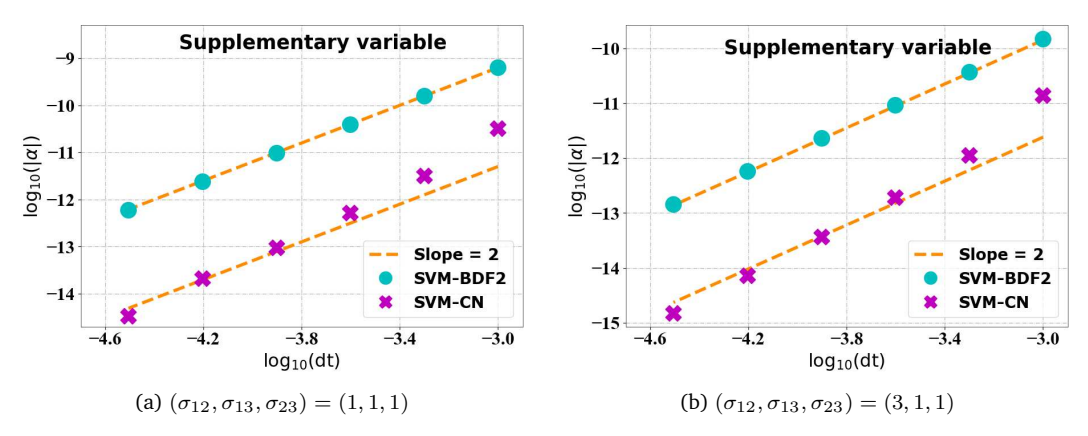


Figure 2: The error plots of supplementary variable, where the surface tension parameters (a): $(\sigma_{12},\sigma_{13},\sigma_{23})=(1,1,1)$ and (b): $(\sigma_{12},\sigma_{13},\sigma_{23})=(3,1,1)$. The slopes of the supplementary variable α error curves for the SVM-BDF2 and SVM-CN schemes are asymptotically close to 2.

We pick the uniform meshes $N_x=N_y=256$ in 2D domain $\Omega=[0,2]^2, M=10^{-3}$, $\epsilon=0.025, \eta=\rho=1, S=1/\epsilon$ and $\Lambda=7$. We conduct these simulations with two sets of surface tension parameters, where one is the partial spreading case $(\sigma_{12},\sigma_{13},\sigma_{23})=(1,1,1)$ and the other is the total spreading case $(\sigma_{12},\sigma_{13},\sigma_{23})=(1,3,1)$.

The time evolution curves of the energy with various time step sizes by EQ-BDF2 with $(S=1/\epsilon)$ / without (S=0) stabilizer and SVM-BDF2 with $(S=1/\epsilon)$ / without (S=0) stabilizer are displayed in Figs. 3 and 4. By comparisons, the curve of energy for the pure un-stabilized EQ-BDF2 blows up for large time step sizes and only decays for $\tau=4.8828125\times 10^{-4}$ in Fig. 3(a). In Fig. 3(c), all the energy curves of SVM-BDF2 without stabilization term monotonically decay except for the ones with time step sizes $\tau\geq 3.90625\times 10^{-3}$. Further, we apply the two schemes with stabilization terms to perform the same test. One can observe that SVM-BDF2 and IEQ-BDF2 with stabilization parameters monotonically decay to the equilibrium state even for the largest time step size $\tau=3.90625\times 10^{-3}$. This shows that both the IEQ-BDF2 scheme and the SVM-BDF2 scheme can provide "stabilize" at relatively large time step sizes. Furthermore, the energy curves at $t=7.8125\times 10^{-3}$ for the IEQ-BDF2 and SVM-BDF2 schemes are

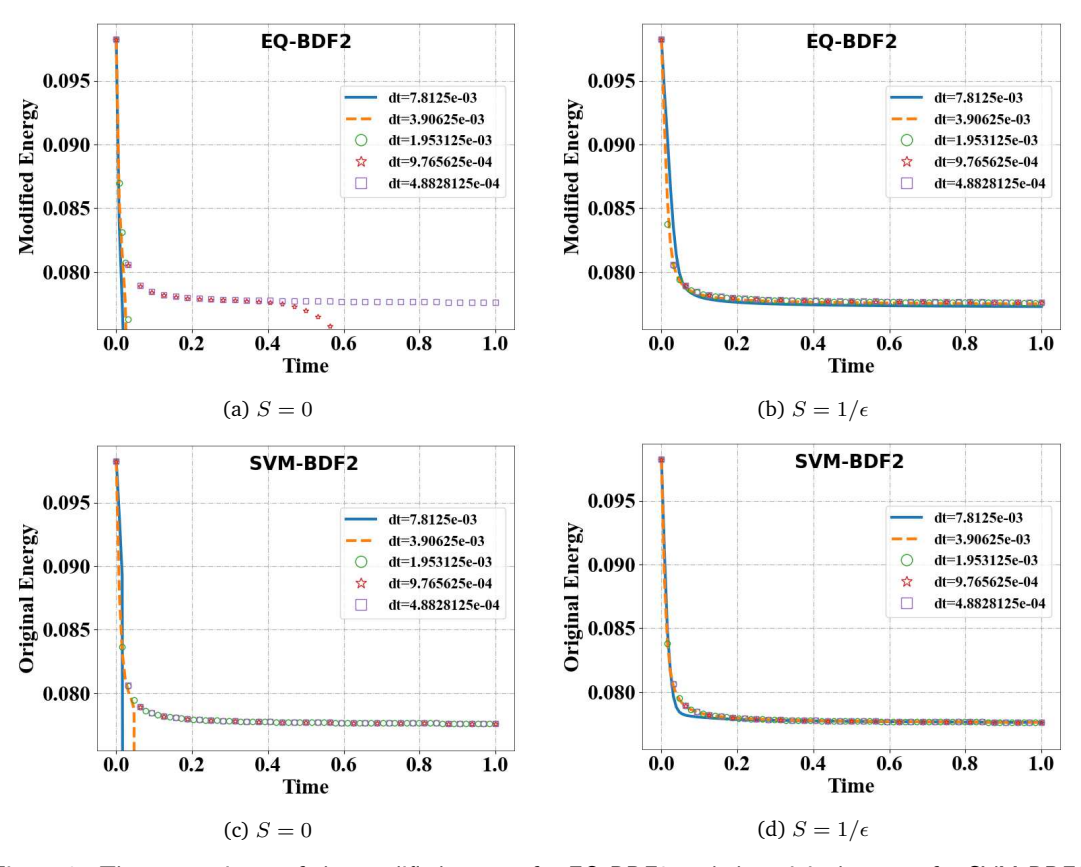


Figure 3: The comparisons of the modified energy for EQ-BDF2 and the original energy for SVM-BDF2 evolution in time with various time steps, where the surface tension parameters $(\sigma_{12}, \sigma_{13}, \sigma_{23}) = (1, 1, 1)$.

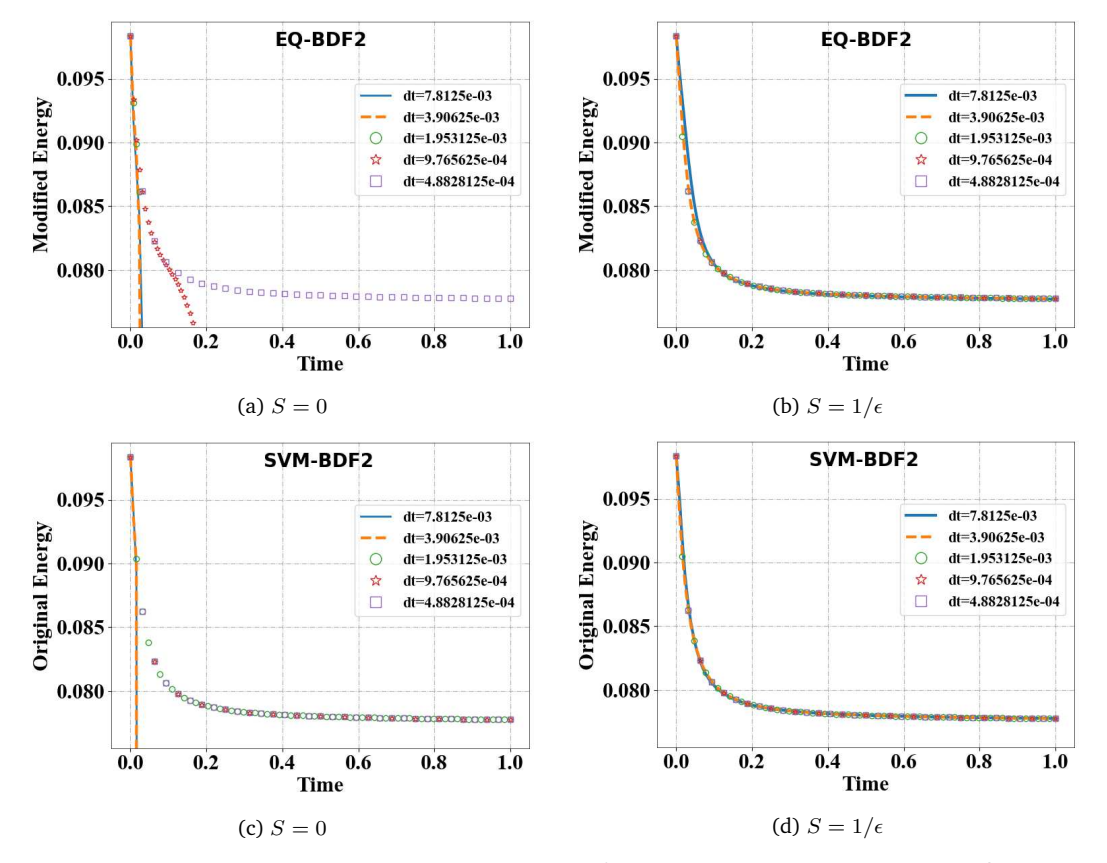


Figure 4: The comparisons of the modified energy for EQ-BDF2 and the original energy for SVM-BDF2 evolution in time with various time steps, where the surface tension parameters $(\sigma_{12}, \sigma_{13}, \sigma_{23}) = (1, 3, 1)$.

away from others, even though they are dissipation. This implies that the stabilization term can improve the numerical stability of the two schemes when the large time step is adopted. As a result, we will select a fixed stabilization parameter $S=1/\epsilon$ to better capture dynamics and accuracy in the subsequent numerical simulations. It is worth noting that our proposed SVM-BDF2 scheme preserves the original energy instead of the modified energy. Meanwhile, we also test the property of mass conservation. From Fig. 5, one can observe that both SVM-BDF2 and SVM-CN warrant the mass of each phase.

Next, we continue to compare the results of the different calculations at t=1 with a fixed step size $\tau=1.0\times 10^{-3}$ in which EQ-BDF2 and SVM-BDF2 equipped with the stabilization parameter $S=1/\epsilon$. Here, we only select the partial spreading case as an example to show the numerical performances. Since the analytic solution is unknown, we choose the solution obtained with time step size $\tau=1.0\times 10^{-7}$ computed by the fully implicit BDF2 scheme as the approximate solution for computing errors. The L^∞ errors of all schemes are summarized in Table 1. Some observed results are listed from these data. The L^∞ error of SVM-BDF2 is smaller than the EQ-BDF2 for all

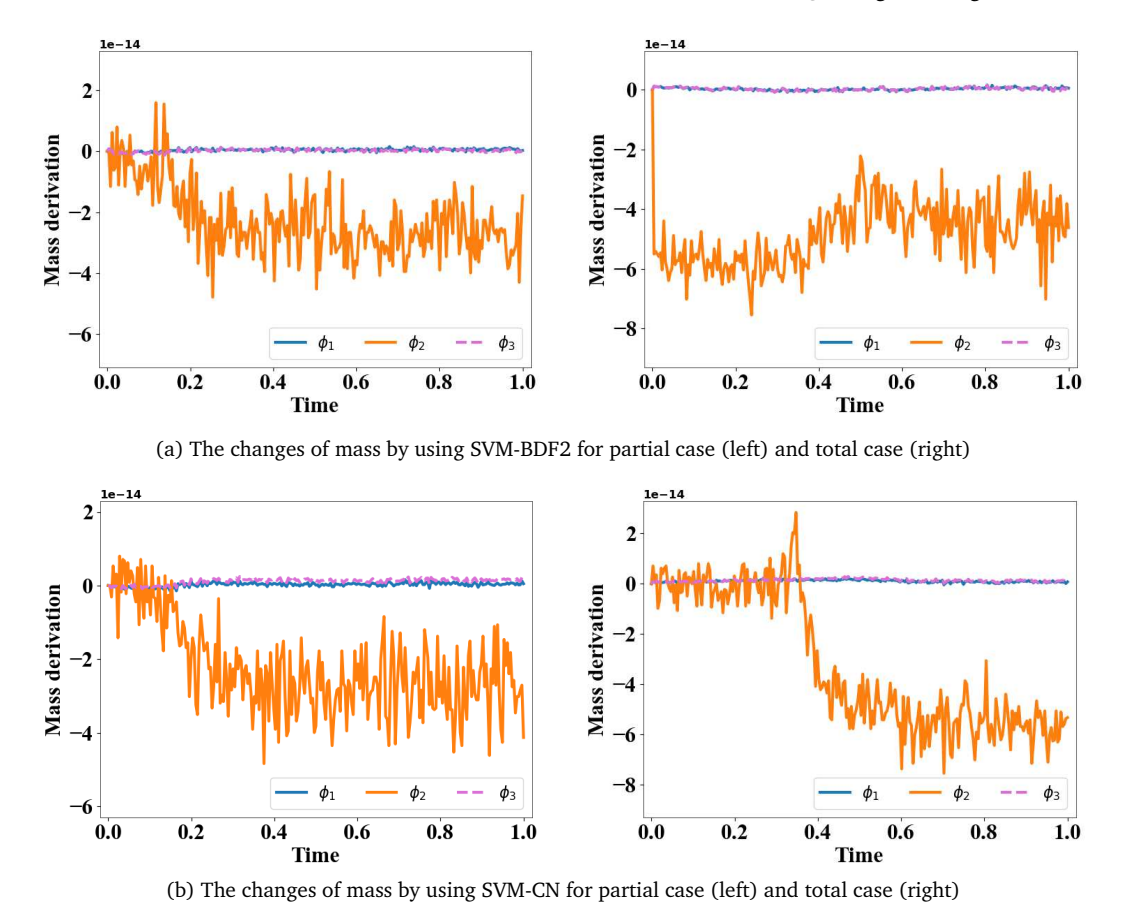


Figure 5: The evolution of mass for each phase by using the SVM-BDF2 and SVM-CN schemes with $S=1/\epsilon$ and the time step $\tau=3.90625\times 10^{-3}$. The curves of the mass derivation show that our proposed schemes preserve mass conservation.

variables. Although we cannot theoretically prove the energy dissipation law for the fully implicit BDF2 scheme, its accuracy performs the best among the three schemes.

Finally, to further illustrate the effectiveness of our proposed scheme, we compare the number of iterations between SVM-BDF2 and fully implicit BDF2. The numerical results are depicted in Fig. 6, where the maximum iterative step is fixed to M=100

Table 1: Numerical comparisons of L^∞ errors for the velocity field and phase field variables at t=1 calculated by the EQ-BDF2, SVM-BDF2 and fully implicit BDF2 schemes by using the fixed time step size $\tau=1\times 10^{-3}$.

Scheme	The partial spreading case	
	L^{∞} error for ${f u}$	L^∞ error for $oldsymbol{\phi}$
EQ-BDF2	3.65e-06	3.23e-03
SVM-BDF2	1.36e-08	1.04e-05
Fully implicit BDF2	3.97e-09	2.32e-06

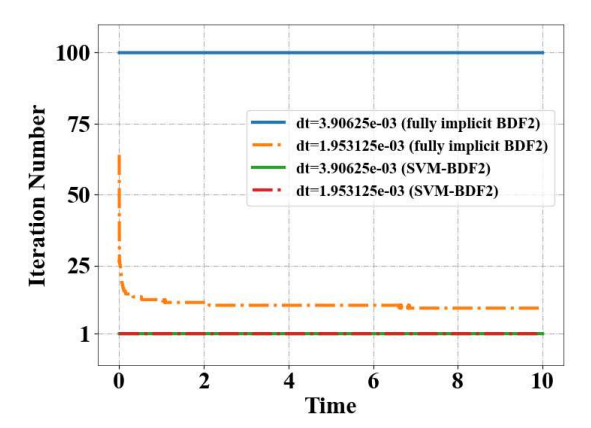


Figure 6: Comparisons of the number of iterations calculated by the fully implicit BDF2 and SVM-BDF2 schemes.

in this simulation. It is discovered that fully implicit BDF2 does not converge at $\tau=3.90625\times 10^{-3}$ even when it reaches our predetermined maximum iteration step. In contrast, our developed scheme is predictably stable and performs more efficiently than the fully implicit BDF2. In a word, the above numerical results strongly suggest that the SVM-BDF2 scheme possesses some advantages.

Example 5.3 (Coarsening dynamics in 2D and 3D). Next, we investigate how the surface tension parameters affect the coarsening dynamics under hydrodynamical environments. We use the domain $\Omega = [0,1] \times [0,2]$ with the uniform spatial meshes 128×256 . We take the parameters as $\rho = \eta = 1$, $\epsilon = 0.025$, S = 40, $\Lambda = 7$ and $M = 10^{-3}$. The initial velocity is set as zero, and we set a random initial condition for the phase variable, which is given by

$$\phi_1(x, y, 0) = 0.5 \left(\frac{y}{4} + 0.25\right) + 0.001 \text{rand}(x, y),$$
 (5.2)

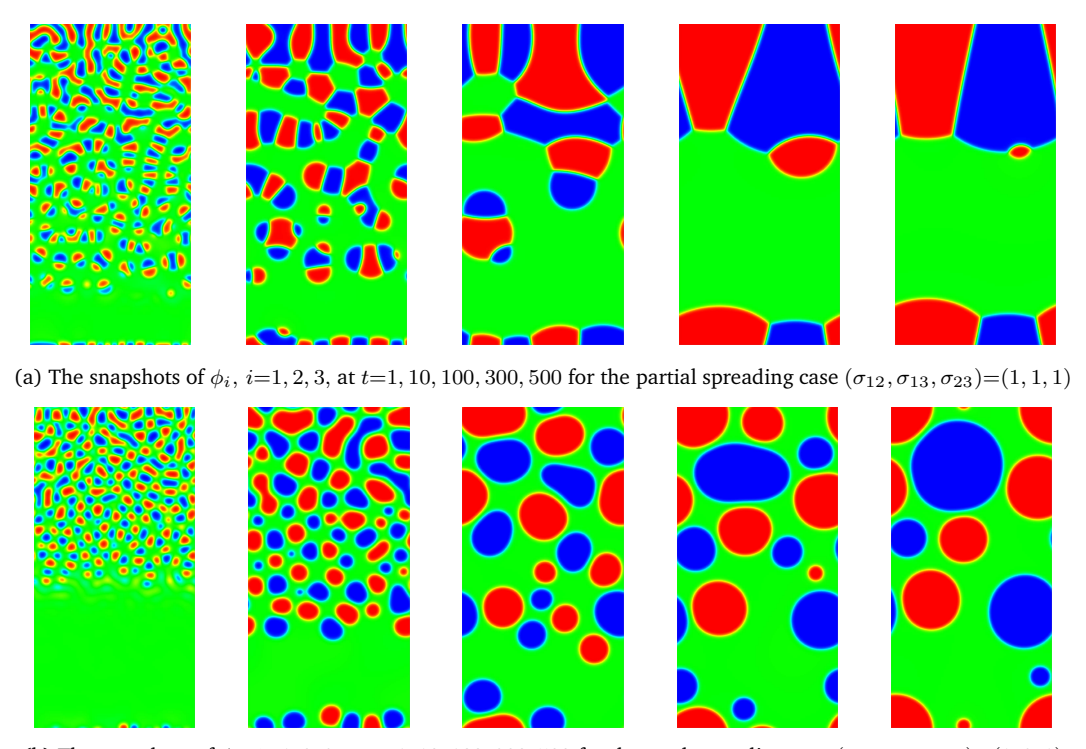
$$\phi_3(x, y, 0) = 0.5 \left(\frac{y}{4} + 0.25\right) + 0.001 \text{rand}(x, y),$$
 (5.3)

$$\phi_2(x, y, 0) = 1 - \phi_1(x, y, 0) - \phi_3(x, y, 0), \tag{5.4}$$

where rand generates the random numbers uniformly distributed in [-1,1]. The second-order SVM scheme is adopted to perform these simulations, including the partial spreading case $(\sigma_{12}, \sigma_{13}, \sigma_{23}) = (1,1,1)$ and the total spreading case $(\sigma_{12}, \sigma_{13}, \sigma_{23}) = (1,3,1)$. For better resolution for all cases, we choose the time step $\tau = 2.5 \times 10^{-3}$ to conduct this simulation respectively.

The 2D simulation results of the phase variables $\phi_i(x,y,t)$, i=1,2,3, at a sequence of time instants, t=1,50,100,300,500, are displayed in Fig. 7. Fig. 7(a) shows blockshaped patterns for the partial spreading case. However, for the total spreading case, one can observe that no junction points are formed, and they become several circles in Fig. 7(b). These results agree with those obtained in [35,36].

Finally, the evolution curves of the original energy and the supplementary variable $\alpha(t)$ as functions of time with $\tau=2.5\times10^{-3}$ up to time T=500 for both cases are



(b) The snapshots of ϕ_i , i=1, 2, 3, at t=1, 10, 100, 300, 500 for the total spreading case $(\sigma_{12}, \sigma_{13}, \sigma_{23})$ =(1, 3, 1)

Figure 7: The 2D time evolution of phase variables ϕ_i (i=1,2,3) with different surface tension, where red, green, and blue represent ϕ_1 , ϕ_2 and ϕ_3 , respectively.

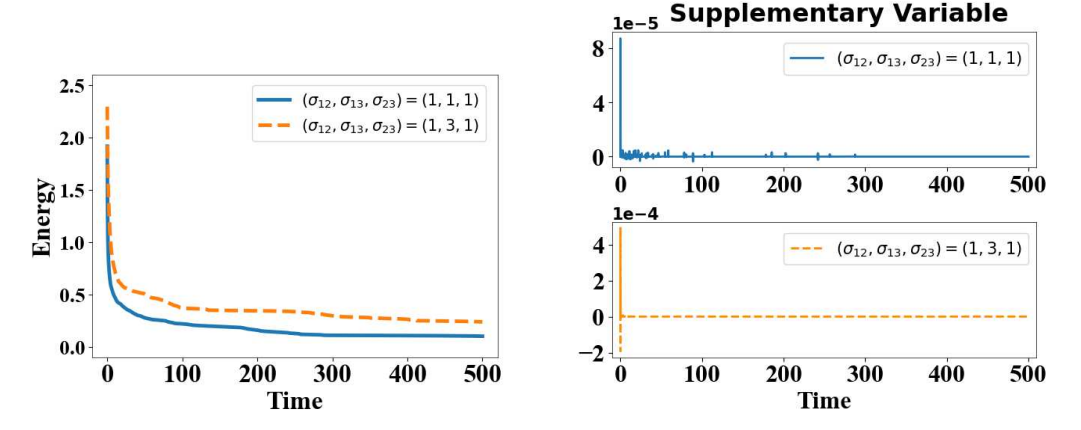


Figure 8: Time evolution of total energy and supplementary variable for 2D coarsening dynamics of the ternary system with the partial spreading and total spreading cases.

graphed in Fig. 8, which verifies that the proposed scheme preserves the original energy dissipation law. Moreover, it indicates that the supplementary variables remain near zero except at a few initial time spots. Fig. 9 plots the corresponding evolution of the mass, which implies the mass is still conserved and validates our theory in The-

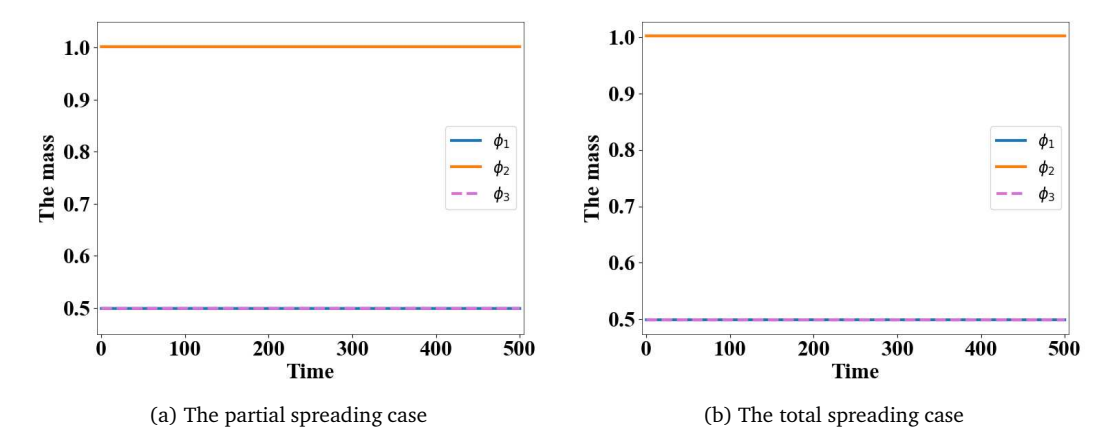


Figure 9: The evolution of the mass for 2D coarsening dynamics of the ternary system with the partial spreading case and total case. This figures show the proposed SVM-BDF2 scheme preserves the mass conservation.

orem 3.1. This numerical experiment demonstrates that among the overall numerical performance of the schemes, the SVM schemes tend to be more efficient, allowing larger time steps.

For 3D phase separation, we use the newly proposed SVM-BDF2 scheme with the same parameters as that used in 3D, except now the computational domain $\Omega = [0, L_x] \times [0, L_y] \times [0, L_z]$ with $L_x = 1, L_y = 1$ and $L_z = 2$. The initial condition reads

$$\phi_1(\mathbf{x}, 0) = 0.5 \left(\frac{z}{2L_z} + 0.25\right) + 0.001 \text{rand}(\mathbf{x}),$$
 (5.5)

$$\phi_3(\mathbf{x}, 0) = 0.5 \left(\frac{z}{2L_z} + 0.25\right) + 0.001 \text{rand}(\mathbf{x}),$$
(5.6)

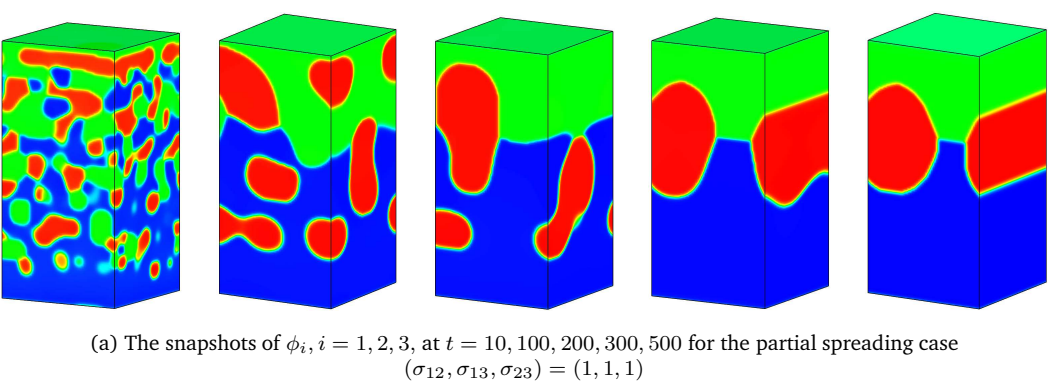
$$\phi_2(\mathbf{x}, 0) = 1 - \phi_1(\mathbf{x}, 0) - \phi_3(\mathbf{x}, 0). \tag{5.7}$$

In the implementation we use $64\times64\times128$ spatial meshes and time step size $\tau{=}2.5\times10^{-3}$. The evolutions of the phase-field variable ϕ_i , $i{=}1,2,3$, in 3D are displayed in Fig. 10. It is interesting to note that our three-dimensional numerical simulations can capture some of the similar configuration shapes observed in the experiments and two-dimensional simulations.

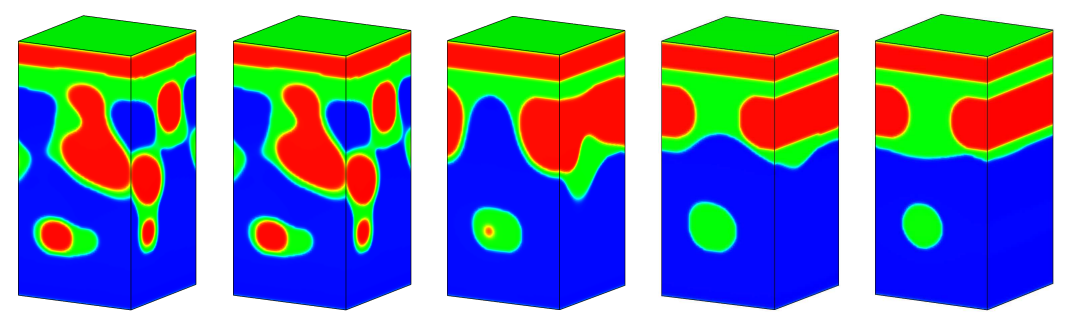
In Fig. 11, we plot the evolution of the original energy. It has been observed that the original energy is decreasing in time, and the supplementary variables are accurate.

Example 5.4 (The effect of surface tension). In this example, we conduct several numerical simulations on the evolutional dynamics of two closed circles driven by surface tension and shear flow. The velocity field is set as $\mathbf{u}(x,y,0)=0$ and the initial conditions for phase variables are provides as

$$\phi_1(x, y, 0) = 0.5 + 0.5 \tanh\left(\frac{0.22 - \sqrt{(x - 0.8)^2 + (y - 0.6)^2}}{\epsilon}\right),$$
 (5.8)



 $(\sigma_{12},\sigma_{13},\sigma_{23})=(1,1,1)$



(b) The snapshots of $\phi_i, i=1,2,3,$ at t=10,100,200,300,500 for the partial spreading case $(\sigma_{12}, \sigma_{13}, \sigma_{23}) = (1, 3, 1)$

Figure 10: The 3D time evolution of phase variables ϕ_i (i=1,2,3) with different surface tension, where the color red, green, and blue represents ϕ_1 , ϕ_2 and ϕ_3 , respectively.

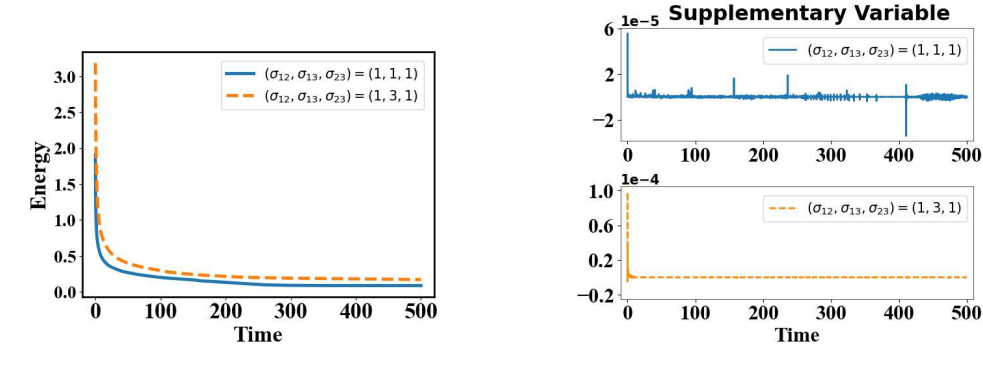


Figure 11: Time evolution of total energy and supplementary variable for 3D coarsening dynamics of the ternary system with the partial spreading and total spreading cases.

$$\phi_2(x, y, 0) = 0.5 + 0.5 \tanh\left(\frac{0.22 - \sqrt{(x - 1.2)^2 + (y - 0.4)^2}}{\epsilon}\right),$$

$$\phi_3(x, y, 0) = 1 - \phi_1(x, y, 0) - \phi_2(x, y, 0),$$
(5.10)

where the initial profiles of the phase variables are plotted in Fig. 12. The domain

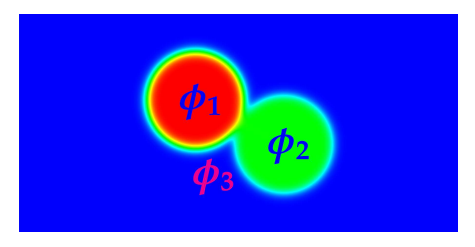


Figure 12: The 2D initial profiles of the surface tension example where the color in red, green, and blue represents ϕ_1 , ϕ_2 , and ϕ_3 , respectively.

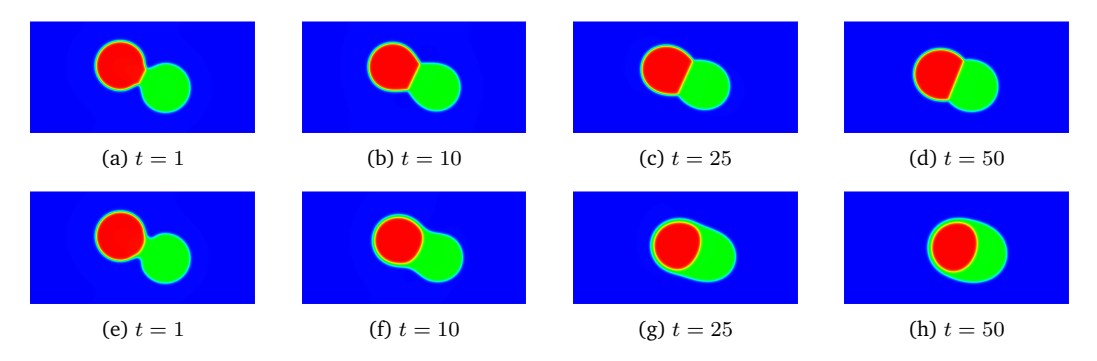


Figure 13: The snapshots of the 2D dynamical evolution for the partial spreading case $(\sigma_{12}, \sigma_{13}, \sigma_{23}) = (1, 1, 1)$ (top) and the total spreading case $(\sigma_{12}, \sigma_{13}, \sigma_{23}) = (1, 3, 1)$ (bottom).

is taken as $\Omega=[0,L_x]\times[0,L_y]$ with $L_x=2$ and $L_y=1$. Some parameters are given by $\rho=1,\ \eta=1,\ \epsilon=0.025,\ M=10^{-3},\ \Lambda=7,S=0.25/\epsilon$. We use uniform grids with $N_x=256$ and $N_y=128$ and time step $\tau=10^{-3}$ to solve this problem. The numerical results for different surface tension are reported in Fig. 13, where the partial spreading case is $(\sigma_{12},\sigma_{13},\sigma_{23})=(1,1,1)$ and the total spreading case is $(\sigma_{12},\sigma_{13},\sigma_{23})=(1,3,1)$. Two circles of the first case join together in the same shapes due to the equal surface tension, while we can observe that the red circle enters into the green circle for the other one.

To further verify the energy stability of the proposed scheme, we also display the original energy evolution dynamics in Fig. 14(a) and the time evolution of the supplementary variable $\alpha(t)$ in Fig. 14(b). We can observe that the energy dissipates in time for both cases and the numerical results of $\alpha(t)$ are accurate.

In the following, we will study how the two kiss-spheres are driven under the shear flow, where the shear is equipped at the bottom and top. This is related to the periodic boundary condition for the velocity at the boundary except at y=0 and $y=L_y$ for which we propose $\mathbf{u}|_{y=0}=(-0.1,0)^T$ and $\mathbf{u}|_{y=L_y}=(0.1,0)^T$. The initial conditions for phase variables are set up as in the previous scenario. The numerical results with different surface tension are summarized in Fig. 15, where the profiles of the phase variable ϕ_i (i=1,2,3) at a sequence of time instants are shown. We observe that the two circles are deformed to form ellipsoids due to the induction of the shear flow. The results demonstrate that our proposed scheme can accurately predict the complicated dynamics of the three-component Cahn-Hilliard-Navier-Stokes system.

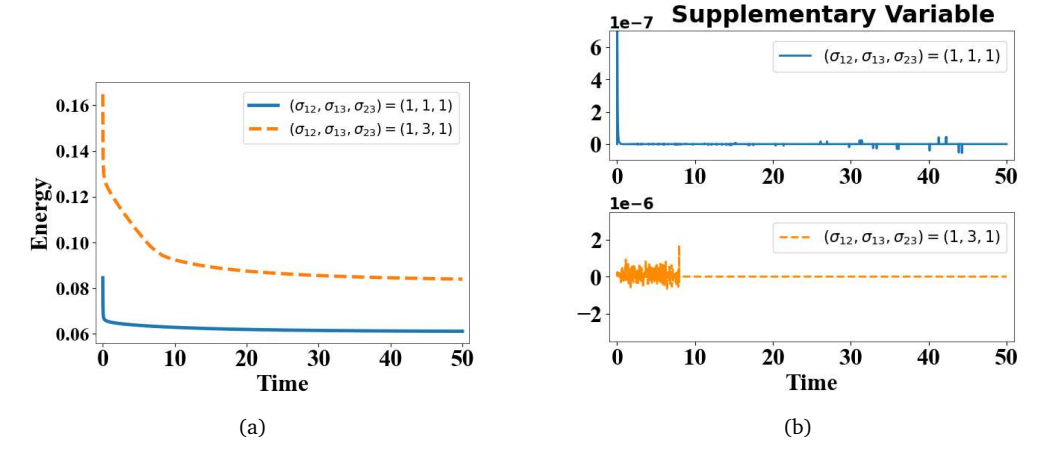


Figure 14: Time evolution of original energy and supplementary variable for the simulations in Fig. 13.

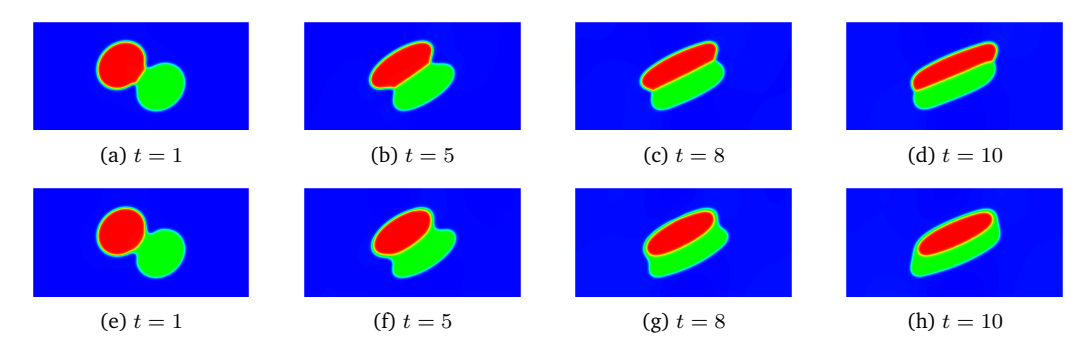


Figure 15: The snapshots of the 2D dynamical evolution that is driven by the shear flow for the partial spreading case $(\sigma_{12},\sigma_{13},\sigma_{23})=(1,1,1)$ (top) and the total spreading case $(\sigma_{12},\sigma_{13},\sigma_{23})=(1,3,1)$ (bottom).

Example 5.5 (Liquid lens under hydrodynamics). In this example, we study fluid lens dynamics driven by the ternary CHNS system, where the lens is located at the interface between two other immiscible fluids [35, 36]. The initial conditions for the phase variables that are shown in Fig. 16 read as

$$\phi_1(x,y,0) = \frac{1}{2} + \frac{1}{2} \tanh \left(\frac{\min(\sqrt{(x-1)^2 + (y-0.5)^2} - 0.15, y-0.5)}{\epsilon} \right),$$
 (5.11)

$$\phi_3(x,y,0) = \frac{1}{2} + \frac{1}{2} \tanh \left(\frac{-\max(0.15 - \sqrt{(x-1)^2 + (y-0.5)^2}, y-0.5)}{\epsilon} \right), \quad (5.12)$$

$$\phi_2(x, y, 0) = 1 - \phi_1(x, y, 0) - \phi_3(x, y, 0), \tag{5.13}$$

and $\mathbf{u}(x,y,0)=\mathbf{0}$. The domain is set up as $\Omega=[0,L_x]\times[0,L_y]$ with $L_x=2$ and $L_y=1$. The periodic boundary conditions are set along the x-direction, the homogeneous Neumann boundary conditions are set for ϕ_i , i=1,2,3, and $\mathbf{u}=(u,v)^T$ along the y-direction except $u|_{y=0}=-\hat{u}_0$, $u|_{y=L_y}=\hat{u}_0$, where \hat{u}_0 represents the magnitude of

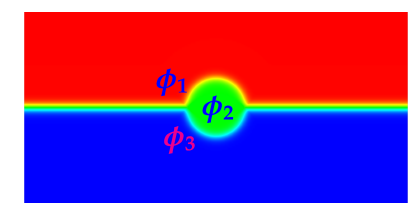


Figure 16: The 2D initial profiles of the Liquid lens example where the color in red, green, and blue represent ϕ_1 , ϕ_2 , and ϕ_3 , respectively.

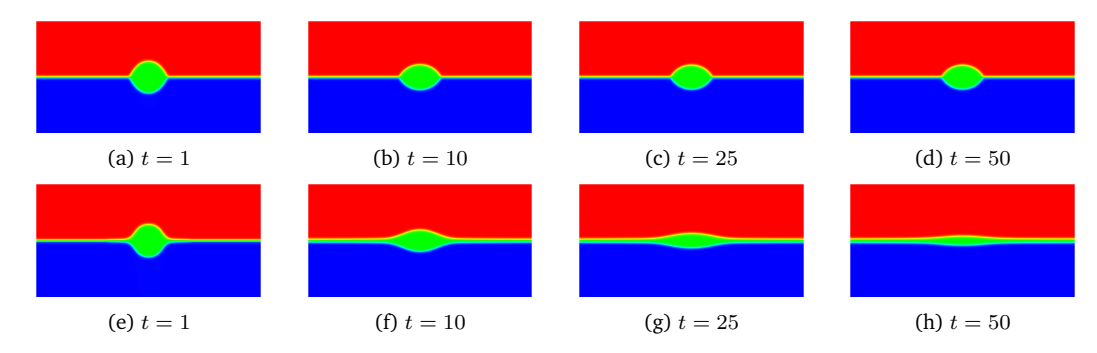


Figure 17: The snapshots of the 2D dynamical evolution that is driven by the shear flow $\hat{u}_0=0$ with different surface tension, i.e., the partial spreading case $(\sigma_{12},\sigma_{13},\sigma_{23})=(1,1,1)$ (top) and the total spreading case $(\sigma_{12},\sigma_{13},\sigma_{23})=(1,3,1)$ (bottom).

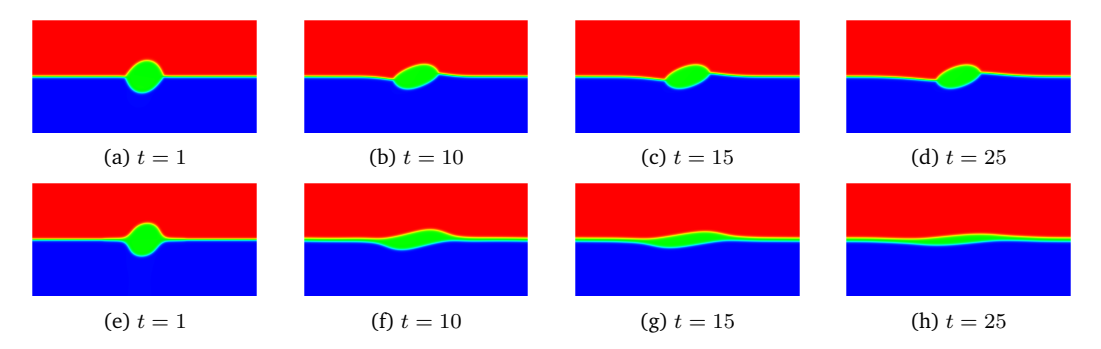


Figure 18: The snapshots of the 2D dynamical evolution that is driven by the shear flow $\hat{u}_0=0.1$ with different surface tension, i.e., the partial spreading case $(\sigma_{12},\sigma_{13},\sigma_{23})=(1,1,1)$ (top) and the total spreading case $(\sigma_{12},\sigma_{13},\sigma_{23})=(1,3,1)$ (bottom).

the shear flow. The parameters are chosen as $M{=}2.5{\times}10^{-3}$, $\epsilon{=}0.025$, $\eta{=}\rho{=}1$, $S{=}0.25/\epsilon$ and $\Lambda=7$. To solve this problem, we use uniform spatial meshes with $N_x=256$ and $N_y=128$, and the time step size is chosen as $\tau=1.0\times10^{-3}$. Moreover, different surface tension coefficients are picked. Fig. 17 reports the numerical results with partial and total cases. For the no-shear case, we observe that the numerical results agree well with the theoretical predictions for the contact angles under no shear flow and are qualitatively consistent with the reported literature [2, 35, 36]. However, introducing the shear flow scenario, the shape of the liquid lens is deformed in Fig. 18.

Example 5.6 (Dynamics of rising drops). In this example, we simulate buoyancy-driven dynamics using the Boussinesq approximation, which means the difference in density between different fluid components is small. Interested readers can refer to [24]. The extra buoyancy term $-(\rho_1\phi_1+\rho_2\phi_2+\rho_3\phi_3-\rho)\mathbf{g}_0$ to the momentum balance equation to approximate the upward force of buoyancy due to the density difference, where ρ is the background density, ρ_i is the density of each phase ϕ_i , i = 1, 2, 3, and \mathbf{g}_0 is the gravity acceleration. We set $ho=
ho_2$ for brevity in this study. The 3D computation domain $\Omega = [0,L_x] \times [0,L_y] \times [0,L_z]$ with $L_x = 1$, $L_y = 1$ and $L_z = 2$ is divided uniformly with step size $h_x = h_y = h_z = 1/128$. The initial velocity is set as zero, and the initial conditions for each phase read

$$\phi_1(x, y, z, 0) = 0.5 + 0.5 \tanh\left(\frac{0.15 - \sqrt{(x - 0.5)^2 + (y - 0.5)^2 + (z - 0.3)^2}}{\epsilon}\right), \quad (5.14)$$

$$\phi_3(x, y, z, 0) = 0.5 + 0.5 \tanh\left(\frac{0.15 - \sqrt{(x - 0.5)^2 + (y - 0.5)^2 + (z - 0.6)^2}}{\epsilon}\right), \quad (5.15)$$

$$\phi_3(x, y, z, 0) = 0.5 + 0.5 \tanh\left(\frac{0.15 - \sqrt{(x - 0.5)^2 + (y - 0.5)^2 + (z - 0.6)^2}}{\epsilon}\right), \quad (5.15)$$

$$\phi_2(x, y, 0) = 1 - \phi_1(x, y, 0) - \phi_3(x, y, 0), \tag{5.16}$$

$$\mathbf{u}(x, y, 0) = \mathbf{0}.\tag{5.17}$$

The model parameters are chosen below

$$\rho_1 = 0.9, \qquad \rho_3 = 1.0, \qquad \rho = 0.9,
\mathbf{g}_0 = (0, 0, 4.98)^T, \quad M = 10^{-3}, \quad \epsilon = 0.018, \quad \eta = 1.$$
(5.18)

This performs a lighter fluid drop immersed in a heavier fluid. Two sets of surface tension parameters are tested, where one is the partial spreading case with $(\sigma_{12}, \sigma_{13}, \sigma_{23}) =$ (1,1,1), and the other is the total spreading case with $(\sigma_{12},\sigma_{13},\sigma_{23})=(1,3,1)$. For the former shown in Fig. 19, the two spheres are finally bound together with identical shapes and rise. In contrast, the other scenario displayed in Fig. 20 presents a different pattern in which the two drops gradually are kept from each other as they ascend.

6. Conclusions

This paper introduces a supplementary variable method with constrained optimization to devise efficient and thermodynamically consistent numerical approximations to solve the hydrodynamically coupled ternary-component Cahn-Hilliard-Navier-Stokes model, which combines the stabilization skill and implicit-explicit treatments for the nonlinear terms. Our approach naturally leads to second-order, efficient, and original energy stable numerical schemes. The resultant schemes only require solving constant and time-independent coefficient matrices that can be pre-computed in addition to a small price for solving a scalar nonlinear equation. Most importantly, the proposed SVM-BDF2 scheme warrants the original energy law, which differs from some popular schemes based on IEQ, SAV, and Lagrange multiplier. In simulating several 2D and 3D

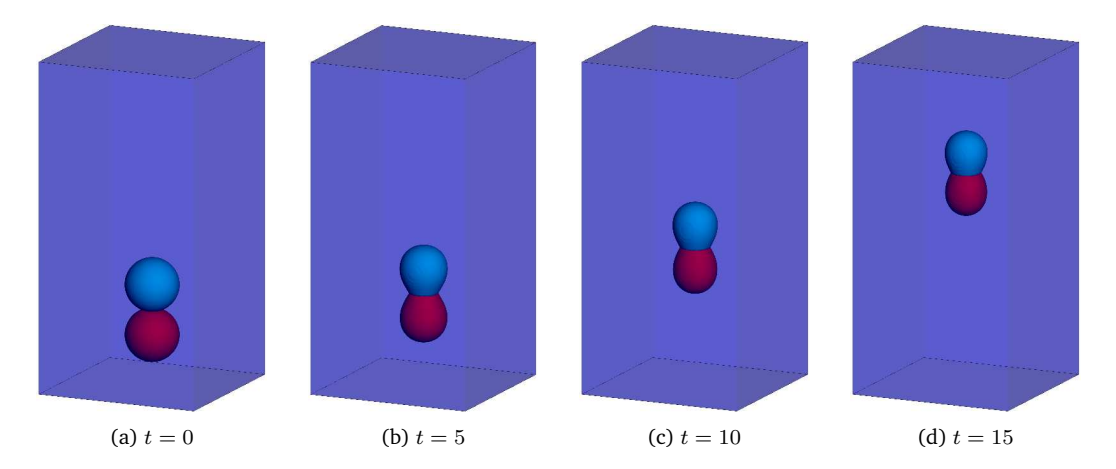


Figure 19: The 3D dynamical evolution of rising bubbles by a buoyancy force with $\mathbf{g}_0 = (0, 0, 4.98)^T$ and the partial spreading case $(\sigma_{12}, \sigma_{13}, \sigma_{23}) = (1, 1, 1)$, at a sequence of time instants t = 0, 5, 10, 15.

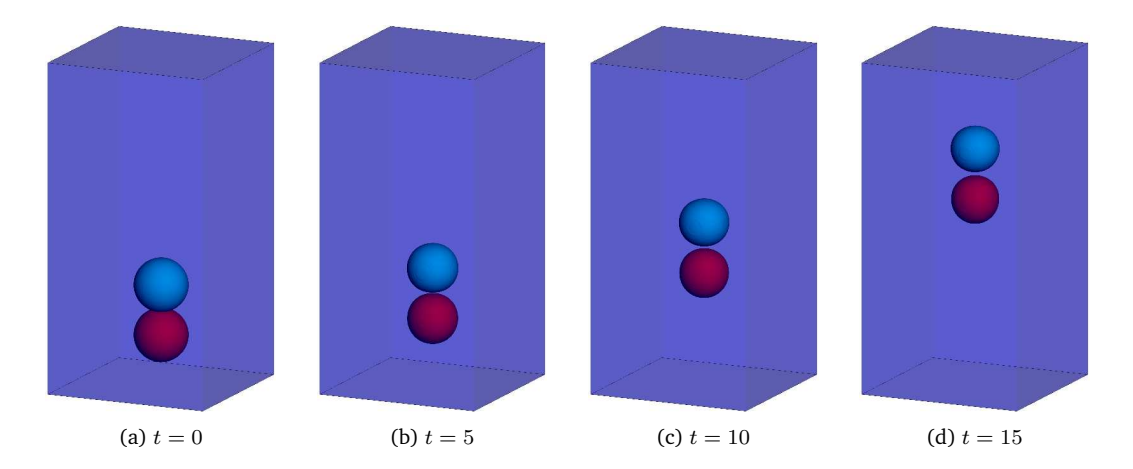


Figure 20: The 3D dynamical evolution of rising bubbles by a buoyancy force with $\mathbf{g}_0 = (0,0,4.98)^T$ and the total spreading case $(\sigma_{12},\sigma_{13},\sigma_{23}) = (1,3,1)$, at a sequence of time instants t=0,5,10,15.

numerical examples and benchmark problems, we demonstrate the stability and accuracy of the developed schemes. The proposed SVM optimization idea is not limited to the ternary CHNS system and its extensions to other coupled thermodynamic and hydrodynamic models will be pursued in our later research.

Acknowledgments

Qi Hong's research is partially supported by the National Natural Science Foundation of China (Grant No. 12201297) and by the LCP Fund for Young Scholar (Grant No. 6142A05QN22005). Yuezheng Gong's research is partially supported by the Foundation of Jiangsu Key Laboratory for Numerical Simulation of Large Scale Complex

Systems, China (Grant No. 202002), by the Fundamental Research Funds for the Central Universities (Grant No. NS2022070), by the Natural Science Foundation of Jiangsu Province (Grant No. BK20220131) and by the National Natural Science Foundation of China (Grant Nos. 12271252, 12071216). Jia Zhao's research is partially supported by the National Science Foundation (NSF) USA with DMS-2111479.

References

- [1] S. BOYAVAL, T. LELIEVRE, AND C. MANGOUBI, Free-energy-dissipative schemes for the Oldroyd-B model, ESAIM Math. Model. Numer. Anal. 43(3) (2009), 523–561.
- [2] F. BOYER AND C. LAPUERTA, *Study of a three component Cahn-Hilliard flow model*, ESAIM Math. Model. Numer. Anal. 40 (2006), 653–687.
- [3] F. BOYER AND S. MINJEAUD, Numerical schemes for a three component Cahn-Hilliard model, ESAIM Math. Model. Numer. Anal. 45 (2011), 697–738.
- [4] L. Chen, *Phase-field modeling for microstructure evolution*, Annu. Rev. Mater. Sci. 32 (2002), 113–140.
- [5] W. CHEN, C. WANG, S. WANG, X. WANG, AND S. WISE, Energy stable numerical schemes for ternary Cahn-Hilliard system, J. Sci. Comput. 84(2) (2020), 27.
- [6] Y. Chen and J. Shen, Efficient, adaptive energy stable schemes for the incompressible Cahn-Hilliard Navier-Stokes phase-field models, J. Comput. Phys. 308 (2016), 40–56.
- [7] Q. CHENG, C. LIU, AND J. SHEN, *A new Lagrange multiplier approach for gradient flows*, Comput. Methods Appl. Mech. Engrg. 367 (2020), 113070.
- [8] L. DONG, C. WANG, S. WISE, AND Z. ZHANG, A positive-preserving, energy stable scheme for a ternary Cahn-Hilliard system with the singular interfacial parameters, J. Comput. Phys. 442 (2021), 110451.
- [9] D. EYRE, *Unconditionally gradient stable time marching the Cahn-Hilliard equation*, MRS Online Proceedings Library 529 (1998), 39–46.
- [10] H. GARCKE, B. NESTLER, AND B. STOTH, A multiphase field concept: Numerical simulations of moving phase boundaries and multiple junctions, SIAM J. Appl. Math. 60 (2000), 295–315.
- [11] Y. Gong, Q. Hong, and Q. Wang, Supplementary variable method for the thermodynamically consistent partial differential equations, Comput. Methods Appl. Mech. Engrg. 381 (2021), 113746.
- [12] Z. Guo, Q. Cheng, P. Lin, C. Liu, and J. Lowengrub, Second order approximation for a quasiincompressible Navier-Stokes Cahn-Hilliard system of two-phase flows with variable density, J. Comput. Phys. 448 (2022), 110727.
- [13] Z. Guo, P. Lin, J. Lowengrub, and S. Wise, Mass conservative and energy stable finite difference methods for the quasi-incompressible Navier-Stokes-Cahn-Hilliard system: Primitive variable and projection-type schemes, Comput. Methods Appl. Mech. Engrg. 326 (2017), 144–174.
- [14] Q. Hong, Y. Gong, J. Zhao, and Q. Wang, Arbitrarily high order structure-preserving algorithms for the Allen-Cahn model with a nonlocal constraint, Appl. Numer. Math. 170 (2021) 321–339
- [15] Q. Hong, J. Li, and Q. Wang, Supplementary variable method for structure-preserving approximations to partial differential equations with deduced equations, Appl. Math. Lett. 110 (2020), 116576.

- [16] J. Hua, P. Lin, C. Liu, and Q. Wang, Energy law preserving C^0 finite element schemes for phase field models in two-phase flow computations, J. Comput. Phys. 230 (2011), 7115–7131.
- [17] M. JIANG, Z. ZHANG, AND J. ZHAO, Improving the accuracy and consistency of the scalar auxiliary variable (SAV) method with relaxation, J. Comput. Phys. 456 (2022), 110954.
- [18] J. KIM, Phase-field models for multi-component fluid flows, Commun. Comput. Phys. 12 (2012), 613–661.
- [19] J. KIM, K. KANG, AND J. LOWENGRUB, Conservative multigrid methods for ternary Cahn-Hilliard systems, Commun. Math. Sci. 2 (2004), 53–77.
- [20] J. KIM AND J. LOWENGRUB, *Phase field modeling and simulation of three-phase flows*, Interfaces Free. Boundaries 7 (2005), 435–466.
- [21] J. KOU AND S. SUN, Thermodynamically consistent simulation of nonisothermal diffuse-interface two-phase flow with Peng-Robinson equation of state, J. Comput. Phys. 371 (2018), 581–605.
- [22] J. LEE AND J. KIM, A second-order accurate non-linear difference scheme for the N-component Cahn-Hilliard system, Phys. A 387 (2008), 4787–4799.
- [23] D. LI, Z. QIAO, AND T. TANG, Characterizing the stabilization size for semi-implicit Fourier-spectral method to phase field equations, SIAM J. Numer. Anal. 54 (2016), 1653–1681.
- [24] C. LIU AND J. SHEN, A phase field model for the mixture of two incompressible fluids and its approximation by a Fourier-spectral method, Phys. D 179 (2003), 211–228.
- [25] J. SHEN, C. WANG, X. WANG, AND S. M. WISE, Second-order convex splitting schemes for gradient flows with Ehrlich-Schwoebel type energy: Application to thin film epitaxy, SIAM J. Numer. Anal. 50 (2012), 105–125.
- [26] J. Shen and X. Yang, Numerical approximations of Allen-Cahn and Cahn-Hilliard equations, Discrete Contin. Dyn. Syst. 28 (2010), 1669–1691.
- [27] L. SHEN, Z. XU, P. LIN, H. HUANG, AND S. XU, An energy stable C^0 finite element scheme for a phasefield model of vesicle motion and deformation, SIAM J. Sci. Comput. 44 (2022), B122–B145.
- [28] Z. TAN, J. Wu, AND J. YANG, Efficient and practical phase-field method for the incompressible multi-component fluids on 3D surfaces with arbitrary shapes, J. Comput. Phys. 467 (2022), 111444.
- [29] Q. WANG, Generalized Onsager Principle and It Applications, in: Froniter and Progress of Current Soft Matter Research, Springer, (2020), 101–132.
- [30] S. Wise, Unconditionally stable finite difference nonlinear multigrid simulation of the Cahn-Hilliard-Hele-Shaw system of equations, J. Sci. Comput. 44 (2010), 38–68.
- [31] S. Wise, J. Kim, and J. Lowengrub, Solving the regularized strongly anisotropic Cahn-Hilliard equation by an adaptive nonlinear multigrid method, J. Comput. Phys. 226 (2007), 414–446.
- [32] C. Xu and T. Tang, Stability analysis of large time-stepping methods for epitaxial growth models, SIAM J. Numer. Anal. 44 (2006), 1759–1779.
- [33] J. Xu, Y. Li, AND S. Wu, On the stability and accuracy of partially and fully implicit schemes for phase field modelling, Comput. Methods Appl. Mech. Engrg. 345 (2019), 826–853.
- [34] J. YANG AND J. KIM, An unconditionally stable second-order accurate method for systems of *Cahn-Hilliard equations*, Commun. Nonlinear Sci. Numer. Simul. 87 (2020), 105276.
- [35] J. YANG AND J. KIM, Numerical study of the ternary Cahn-Hilliard fluids by using an efficient modified scalar auxiliary variable approach, Commun. Nonlinear Sci. Numer. Simul. 102 (2021), 105923.
- [36] X. YANG, Efficient and energy stable scheme for the hydrodynamically coupled three compo-

- nents Cahn-Hilliard phase-field model using the stabilized-invariant energy quadratization (IEQ), J. Comput. Phys. 438 (2021), 110342.
- [37] X. YANG, Efficient, second-order in time, and energy stable scheme for a new hydrodynamically coupled three components volume-conserved Allen-Cahn phase-field model, Math. Models Methods Appl. Sci. 31 (2021), 753–787.
- [38] X. YANG, J. ZHAO, Q. WANG, AND J. SHEN, Numerical approximations for a three-components Cahn-Hilliard phase-field model based on the invariant energy quadratization method, Math. Models Methods Appl. Sci. 27 (2017), 1993–2030.
- [39] Z. YANG AND S. DONG, An unconditionally energy-stable scheme based on an implicit auxiliary energy variable for incompressible two-phase flows with different densities involving only precomputable coefficient matrices, J. Comput. Phys. 393 (2019), 229–257.
- [40] Z. Yang and S. Dong, A roadmap for discretely energy-stable schemes for dissipative systems based on a generalized auxiliary variable with guaranteed positivity, J. Comput. Phys. 404 (2020), 109121.
- [41] M. Yuan, W. Chen, C. Wang, S. Wise, and Z. Zhang, An energy stable finite element scheme for the three-component Cahn-Hilliard-type model for macromolecular microsphere composite hydrogels, J. Sci. Comput. 87 (2021), 78.
- [42] J. Zhang and X. Yang, Decoupled, non-iterative, and unconditionally energy stable large time stepping method for the three-phase Cahn-Hilliard phase-field model, J. Comput. Phys. 404 (2020), 109115.
- [43] J. ZHANG AND X. YANG, Unconditionally energy stable large time stepping method for the L^2 -gradient flow based ternary phase-field model with precise nonlocal volume conservation, Comput. Methods Appl. Mech. Engrg. 361 (2020), 112743.
- [44] J. Zhao, A revisit of the energy quadratization method with a relaxation technique, Appl. Math. Lett. 120 (2021), 107331.